PAPER

Check for updates

Enhanced H₂ recovery by coupling the water–gas shift reaction with *in situ* CO₂ capture and mineralization using earth abundant Ca- and Mg-silicates and hydroxides†

Xun Gao,[a] Divya Prasad,[a] Mahadeo A. Mahadik[a] and Greeshma Gadikota [iD] *[ab]

Decarbonization of clean energy carriers such as H_2 by coherent integration of multiphase chemical pathways with inherent carbon mineralization is a thermodynamically downhill pathway designed for a sustainable climate, energy, and environmental future. In this effort, a low-temperature water–gas shift reaction (WGSR) with Pt/Al_2O_3 catalysts is integrated with *in situ* carbon mineralization in a multiphase reaction environment. The hypothesis that Pt-based catalysts favor selective formation of H_2 over CH_4 has been investigated. H_2 yields increased by 30.8%, 9.5%, 8.3%, and 1.7% in the presence of $Ca(OH)_2$, $Mg(OH)_2$, Mg_2SiO_4, and $CaSiO_3$ relative to the blank experiment without the sorbent at constant experimental conditions of 250 °C and reaction time of 12 hours in the presence of Pt/Al_2O_3 catalyst with initial CO and N_2 pressures of 8 bar and 12 bar, respectively. These studies unlock the feasibility of advancing single-step multiphase pathways for enhancing H_2 yields with inherent CO_2 capture and mineralization for a low carbon and sustainable energy and resource future.

1. Introduction

Demand for low-cost and abundant fossil energy resources has exacerbated greenhouse gas emissions (GHGs) leading to detrimental impacts on climate and the environment.[1] To mitigate the detrimental impacts of GHG emissions and realize a carbon-neutral future, it is essential to develop novel chemical pathways to produce clean energy carriers such as H_2 while capturing and storing CO_2 emissions.[2,3] As an alternative to conventional multi-step processes to capture, compress, and store CO_2 emissions, intensified approaches that simultaneously inherently capture and store CO_2 emissions in a single step *via* reactive separation are needed.[4,5] The abundance of renewable energy resources such as biomethane serves as a viable feedstock for H_2 production as an alternative to fossil-derived methane. H_2 has emerged as a preferred energy carrier given the high energy density of H_2 (122 MJ kg⁻¹) compared to alternative fossil fuel-derived resources[5] and the absence of CO_2 emissions on combustion.[6]

Current commercial H_2 production involves energy-intensive hydrocarbon reforming, by which the non-renewable hydrocarbon fuel is reformed into carbon monoxide (CO) to release H_2 over metal catalysts.[7] As one of the primary reforming techniques, steam reforming (SR) is widely studied due to its relatively low operating temperature and high purity of the H_2 product.[8] The general reaction for steam reforming can be represented as follows:

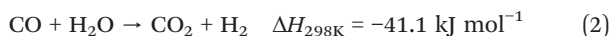$$C_mH_n + mH_2O = mCO + \left(m + \frac{1}{2}n\right)H_2 \quad \Delta H > 0 \qquad (1)$$
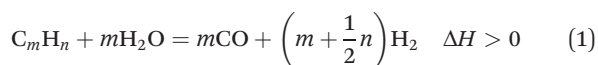
In this expression, when $m = 1$ and $n = 4$, the reforming reaction corresponds to steam methane reforming (SMR), which is the most extensively applied approach for industrial H_2 production with thermal efficiencies of up to 85%.[8] SMR is typically coupled with subsequent water–gas shift reaction (WGSR) and methanation to further enhance H_2 yield and purity.[9] As an effective supplement to SMR, the WGSR generates additional H_2 while simultaneously reducing the concentrations of CO at intermediate temperatures (200–450 °C).[10] The literature review by Wagner on catalytic advancements[11] and fundamental insights on kinetic rates and challenges towards water gas shift are pioneering studies focused on optimizing this reaction.[9,12] Thermodynamically, WGSR is favored at low temperatures because it is a reversible exothermic process using steam as the hydrogen source as eqn (2) indicates:

[a] School of Civil and Environmental Engineering, Cornell University, Ithaca, NY 14853, USA
[b] Smith School of Chemical and Biological Engineering, Cornell University, Ithaca, NY 14853, USA. E-mail: gg464@cornell.edu; Tel: +1 607 255 4796

† Electronic supplementary information (ESI) available. See DOI: https://doi.org/10.1039/d4re00480a

576 | *React. Chem. Eng.*, 2025, **10**, 576–592

This journal is © The Royal Society of Chemistry 2025

$$CO + H_2O \rightarrow CO_2 + H_2 \quad \Delta H_{298K} = -41.1 \text{ kJ mol}^{-1} \qquad (2)$$

However, in the low-temperature regime, WGSR is challenged by sluggish kinetics and low CO conversions. The limiting kinetics of WGSR can be overcome by harnessing catalysts to enhance CO conversion kinetics and yields at low temperatures, for which various noble (Pt, Pd, Ru) and non-metal (Cu, Zn, Fe, Cr)-based supported catalysts have been reported in precedent literature.[13–15] Especially, Pt-based materials have been reported to be promising metals for WGSR in the medium to low temperature (250–350 °C) regime due to their high stability in oxidizing environments.[16]

Even though steam methane reforming and WGSR are widely deployed for H_2 production, challenges associated with producing high-purity H_2 and achieving high selectivity remain.[17] The competing co-presence of CO and CO_2 along with H_2 from gasification and WGSR at the effluent limits H_2 selectivity and its yield. Consequently, the reactor effluent gases must be purified by the pressure swing adsorption process operating at high pressures (1 MPa) to produce a significant amount of high-purity H_2.

This challenge necessitates the development of sustainable multiphase chemical pathways for selective and energy-efficient reactive separation of H_2 from CO_2 and CO. Harnessing alkaline materials such as Ca- and Mg-bearing hydroxides and silicates is a thermodynamically favorable pathway to enhance H_2 yield. The proposed enhanced WGSR concept works based on the Le Chatelier's principle, in which the reversible gas phase WGSR when integrated with a slurry bearing Ca- and Mg-bearing hydroxides and silicates enhances H_2 yield *via in situ* CO_2 capture and mineralization.[18] This integrated concept has the potential to significantly improve reaction efficiencies, minimize capital cost, and simplify the process configuration from the two-step conventional catalytic process to a single – step process. This approach also circumvents the thermodynamic limitations of conventional WGSR thereby enhancing the rate of forward reaction for H_2 generation, driving the reaction towards the product side by shifting the equilibrium, and allowing high conversions of CO and steam to H_2 and solid carbonates.

The approach of coupling carbon mineralization as a pathway to capture and crystallize CO_2 emissions as solid carbonates is a significant departure from conventional carbon capture and storage (CCS) technologies in which CO_2 is first captured using solvents, sorbents, and membranes and is then injected into geologic reservoirs for storage.[19–23] The permanence and stability of solid Ca- and Mg-bearing carbonates[24] motivate the coupling of carbon mineralization as a pathway to separate CO_2 emissions and enhance H_2 yields. Table 1 summarizes the state-of-the-art literature reports focused on the enhancement towards WGS performance and H_2 yields.[18,25–33]

Carbon mineralization involves the reaction between silicate, hydroxide, and oxide minerals bearing divalent cations (*e.g.*, Ca^{2+}, Mg^{2+} ions) and CO_2 to produce the respective carbonates. The negative free energy change of the reaction indicates the spontaneity of the process and the chemical stability of the carbonate products.[34] Apart from the spontaneity of the reaction, carbon mineralization has several advantages. First, the natural abundance of starting materials guarantees easy accessibility and affordable prices. Besides, the alkaline minerals have a large CO_2 storage capacity, providing an enormous CO_2 storage potential worldwide. Additionally, the typical products from carbon mineralization, including silica, carbonates, and metal oxides, usually have multiple industrial applications after purification.

For carbon mineralization, the starting materials could be magnesium silicate minerals such as $(Mg,Fe)_2SiO_4$ (olivine), Mg_2SiO_4 (forsterite), MgO (periclase), CaO (lime), $CaSiO_3$ (wollastonite), and Ca^{2+}- and Fe^{2+}-rich silicates (*e.g.*, larnite). These minerals are known to spontaneously react with atmospheric CO_2 to produce solid carbonates.[35–37] These geo-inspired mineralization pathways motivated advances in

Table 1 Comparative table of enhanced WGS with different sorbents and catalytic systems

Feedstock	Sorbents	Catalyst	Temperature [°C]	Pressure [bar]	Sorbents amount [g]	Catalyst amount [g]	H_2 yields [%]	CO_x yields [%]	Ref.
CO_2, CO, steam, H_2, N_2	LDHs	Iron–chromium	400	28	891	434	99.83	0.17%	18
CO, steam, Ar	LDHs	$Cu/ZnO/Al_2O_3$	400	1	48.45	48.45	99.99	0.01%	25
CO, steam, N_2	CaO/Al_2O_3	Ni nanoparticle	400	NA	0.25	0.0075	76–98	NA	26
CO, steam, N_2	CaO/Al_2O_3	Pt/Al_2O_3	350	NA	NA	NA	High purity	NA	27
CO, steam, Ar	$CaO/Ca_{12}Al_{14}O_{33}$	Fe/Mn	400–700	1	0.88	0.12	88–95	5–12	28
CO, steam	CaO-based	Pd/Ni/Co	425–550	1	20	1	98–99	0.35	29
CO, steam, H_2, He	CaO/NaOH	Pt/ZDC	300–600	1–11	NA	NA	51–100	0–49	30
CO, steam	$AMS/MgO/CaCO_3$	$Cu/Ce_{0.6}Zr_{0.4}O_2$	275–375	12	2.625	2.625	86–99	1–14	31
H_2, CO, steam, N_2	Na–Mg based	$Cu/ZnO/Al_2O_3$	375	1	5	5	High purity	NA	32
CO_2, N_2, H_2	CaO	MO_x (Al, Ce, Ti, Zr)	600–750	NA	0.2	0.1	NA	NA	33
H_2, CO, N_2	Mg/Ca hydroxide and silicate	Pt/Al_2O_3	250–300	20	3	3	72.67	27.33	This work

This journal is © The Royal Society of Chemistry 2025

React. Chem. Eng., 2025, **10**, 576–592 | 577

Paper

engineered analogs to accelerate mineralization.[34,38] Prior work by Gadikota and co-workers showed that olivine carbon mineralization extents as high as 85% are achieved at 185 °C, pCO_2 of 139 atm, reaction time of 3 hours, and in 1.0 M NaCl and 0.64 M $NaHCO_3$ solution with particle sizes of 30 μm or less.[39–41] The observed high extents of carbon mineralization at the temperature conditions that are similar to that of the water gas shift reaction motivated the coupling of this mineralization pathway.

As an alternative to these hydrothermal routes, direct gas – solid mineralization routes[42,43] are explored but challenged by slow kinetics when Mg- or Ca-bearing silicates are used. In this context, sorbent-enhanced water gas shift reactions (WGSR) in direct gas–solid modes were extensively studied.[44–47] Compared with the widely used membrane separation approach to separate CO_2 in WGSR, the sorbent-enhanced WGSR possesses multiple advantages, including more favorable and uniform kinetics, greater material durability, and larger CO_2 capture capacity.[30,48] Conventional sorbent-enhanced water–gas shift reactions occur in fluidized bed reactors with steam-saturated CO_2 flow.[32,49] The selected sorbents are typically metal oxides (*e.g.*, CaO) or layered double hydroxide (LDH) (*e.g.*, hydrotalcite) with high CO_2 capture capacity.[18,25,26] However, direct gas–solid carbonation is very kinetically limited and tends to be greatly enhanced with the participation of aqueous media, which dissolves the alkaline resource to release metal cations that capture CO_2 to form carbonate species.[43,50–52]

While Ca-bearing oxides have been reported to be effective for enhanced water gas shift reaction in a direct gas–solid reaction mode,[27,29,30] the direct use of earth abundant Mg- and Ca-bearing silicates in this mode is significantly challenged by mass transfer limitations and slow kinetics of reaction.[39–41] The direct use of Mg- and Ca-bearing silicates circumvents the need to use additional reagents to produce more reactive Ca- and Mg-bearing hydroxides. To accelerate mass transfer and the kinetics of CO_2 capture using earth-abundant Mg- and Ca-bearing silicates, aqueous routes which involve the dissolution of silicates to release Mg^{2+} or Ca^{2+} ions for capturing CO_2 produced from the WGSR to produce the respective carbonates are investigated in this work.[53] Prior studies have reported that the dissolution of silicate minerals facilitates more robust mass transfer and accelerates carbon mineralization.[54–56] Prior studies have demonstrated enhanced H_2 production using $Mg(OH)_2$ for *in situ* CO_2 capture and mineralization.[57] However, the influence of directly using of Mg- and Ca-bearing silicates for the enhanced water gas shift reaction has not been reported to date. The conventional hypothesis is that silica precipitated as Mg- and Ca-bearing silicates limit mass transfer and thus lower reactivity with CO_2 to produce the respective Ca- and Mg-bearing carbonates. However, this hypothesis has not been evaluated in the context of harnessing earth-abundant Ca- and Mg-bearing silicates to enhance the WGSR with *in situ* CO_2 capture and

mineralization, and is therefore, the focus of the proposed investigations.

Several favorable multiphase chemical interactions are necessary for this approach to be feasible. First, the reactivity of CO and steam in the presence of Pt/Al_2O_3 catalyst needs to be robust in producing CO_2 and H_2 as the products in sufficient quantities. Second, CO_2 needs to be soluble in the aqueous phase to facilitate the forward WGSR for enhancing H_2 production. Third, the dissolved CO_2 needs to react with Mg- and Ca-bearing silicates to produce the respective carbonates. Fourth, the precipitated silica should not limit mass transfer and the subsequent carbon mineralization behavior. To unlock the full potential of enhanced H_2 production coupled with carbon mineralization, it is essential to identify the rate limiting factor and advance strategies to overcome these limitations. To this end, the multiphase reaction pathways are assembled such that the gas phase catalytic WGSR is coupled with slurry phase carbon mineralization as shown in Fig. 1. The associated CO_2 from WGSR reacts with water to produce carbonate species, which subsequently react with dissolved calcium or magnesium ions obtained from the sorbents for *in situ* carbon mineralization. To identify and address the factors limiting H_2 production coupled with carbon mineralization, several key research questions are addressed: (i) what are the chemical mechanisms underlying enhanced H_2 conversion with *in situ* carbon mineralization using Mg- and Ca-bearing

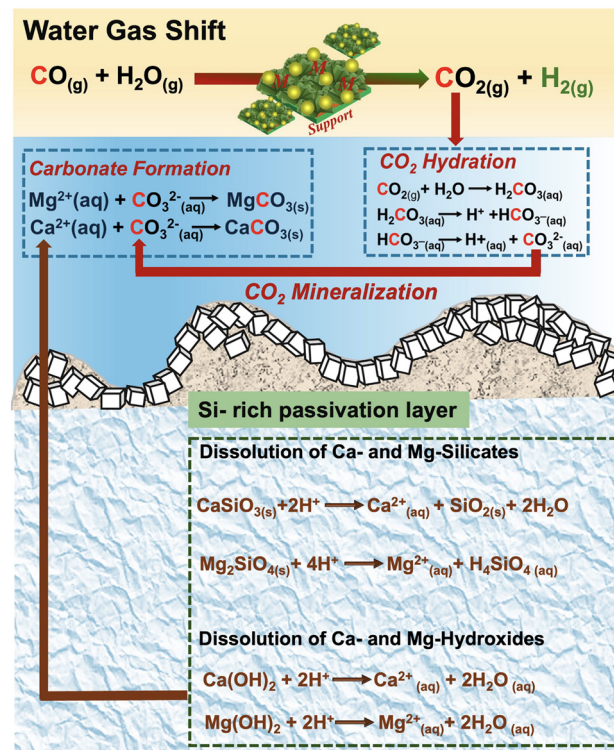**Fig. 1** Schematic representation of the pathway to enhance H_2 conversion by integrating the water gas shift reaction integrated with carbon mineralization of Ca- and Mg-bearing hydroxides and silicates.

hydroxides and silicates? (ii) What is the influence of the silicate *vs.* hydroxide reactivity on enhancing H_2 production with carbon mineralization? (iii) In this multi-step reaction pathway, what is the rate limiting step and how can this step be accelerated?

Addressing these questions unlock new insights into the mechanisms and the scientific feasibility of enhancing H_2 conversion with *in situ* CO_2 capture and mineralization using Mg- and Ca-bearing silicates and contrasting with that of the respective hydroxides.

2. Experimental methods

2.1 Materials and methods

All experiments to investigate enhancement in H_2 conversion with the WGSR coupled with *in situ* CO_2 capture and mineralization are conducted in the presence of platinum on alumina support (Pt/Al_2O_3) catalyst.[27] The Pt/Al_2O_3 catalyst is selected due to its high activity, superior thermal stability, and high product specificity to H_2 and CO_2.[58–60] Specifically, Pt/Al_2O_3 catalyst is sized as 3.2 mm pellets with a composition of 0.5 wt% Pt and is procured from Sigma Aldrich, USA. Mg-bearing hydroxide (brucite ($Mg(OH)_2$)) and silicate (forsterite (Mg_2SiO_4)) used for *in situ* CO_2 capture and mineralization are obtained from Fisher Chemical and Xi'An Function Material Group Co. Ltd, respectively. Ca-bearing hydroxide (portlandite ($Ca(OH)_2$)) and silicate (wollastonite ($CaSiO_3$)) also used for *in situ* CO_2 capture and mineralization are acquired from Thermo Fischer Scientific Co., USA. These Mg- and Ca-bearing silicates and hydroxides are ball-milled in a bench-top mixer mill (8000 M Mixer/Mill® by SPEX® Sample Prep) to obtain raw materials with comparable mean particle sizes (5.57 μm to 10.38 μm). The particle sizes of the milled samples are determined using laser diffraction

particle size analyzer (Anton Paar). Deionized water (18.2 MΩ cm, Millipore) is used throughout all the experiments as required. Ultra-high purity CO gas (99.999% purity) is supplied by Airgas Co., USA.

2.2 Experimental setup for enhanced WGSR and carbon mineralization

Experiments to investigate enhanced H_2 conversion with *in situ* CO_2 capture and mineralization are conducted in a 50 mL stainless steel high-pressure stirred reactor (Micro Bench Top Reactor, Parr Instruments Co., USA) in a multiphase reaction environment. A schematic representation of the experimental setup is shown in Fig. 2. The reactor is a stirred cylindrical system with an inner diameter of 33 mm and a height of 57 mm. It features a 4-blade Rushton turbine stirrer with a 20 mm diameter, positioned 9 mm above the bottom along the central axis of the reactor. Given the stirring rate and the dimensions of the stirrer, efficient mixing and mass transfer in the aqueous phase is expected during the reaction. Simultaneously, CO and N_2 are introduced through a gas inlet pipe (inner diameter of 3 mm) into the headspace for gas-phase reactions and to build internal pressure. Elevated internal pressures are preferred for these multiphase reactions, as the increased CO partial pressure shifts the equilibrium of the WGSR towards higher H_2 and CO_2 production, enhancing the subsequent dissolution and diffusion of CO_2. Catalytic conversion of CO and steam occurs in the gas phase in the presence of Pt/Al_2O_3 catalyst. The surface area, pore volume, and average pore diameter of Pt/Al_2O_3 catalyst are 163.13 m^2 g^{-1}, 0.303 cc g^{-1}, and 6.282 nm, respectively (see Table S1 in ESI†). Prior to CO gas injection, 3 g (0.5 wt%) of the commercial Pt/Al_2O_3 catalyst is placed in an aluminum basket and suspended in the
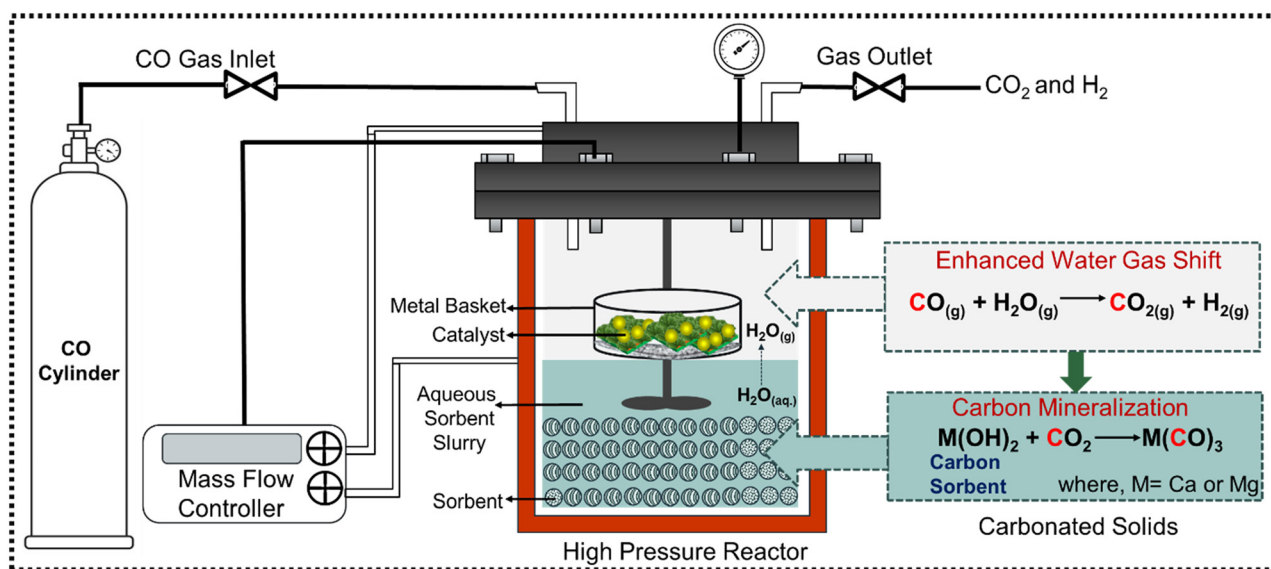

Fig. 2 Schematic representation of the experimental setup for coupling the water gas shift reaction (WGSR) with *in situ* CO_2 capture and mineralization for enhanced H_2 conversion.

This journal is © The Royal Society of Chemistry 2025

React. Chem. Eng., 2025, **10**, 576–592 | **579**

headspace of the reactor ensuring the basket is not in contact with the sorbent slurry. CO flow rate from the cylinder is controlled by using a mass flow controller (MFC). CO_2 capture and mineralization occurs in a slurry phase bearing 3 g of Mg- and Ca-bearing hydroxides and silicates, mixed with 10 mL of deionized water. The initial solid-to-liquid weight ratio is set at 3 : 10, resulting in mole percentages of 8.48% for $Mg(OH)_2$, 3.70% for Mg_2SiO_4, 6.80% for $Ca(OH)_2$, and 4.45% for $CaSiO_3$, respectively. The sorbent-to-catalyst ratio is maintained at a consistent weight ratio of 1 : 1 across all cases.

The headspace of the reactor is purged with CO gas for 15 minutes to evacuate gaseous impurities before it is pressurized and sealed tightly. After reaching the desired pressure set point for CO at 20 bar, the heater is switched on to achieve a setpoint of 250 °C with a constant stirring rate of 300 rpm, signaling the start of the experiment. Steam is generated by the vaporization of water in the slurry. The corresponding partial pressure of steam is determined by the temperature in the steam table (Table S2.1 and 2.2†). The reactor outlet is sealed with heating tape to avoid the possibility of steam condensation and is connected directly to a gas chromatograph to analyze the concentrations of gaseous products. The pH of the slurry increased to 9.95 for $Mg(OH)_2$, 8.69 for Mg_2SiO_4, 12.37 for $Ca(OH)_2$, and 8.98 for $CaSiO_3$, respectively. The experiments are performed at different reaction times ranging from 3 to 12 hours. After the completion of the reaction, the reactor is cooled down to ambient temperature. Following this, the outlet valve is slowly opened to purge the gaseous products in the micro-GC and the carbonate-bearing solid products are collected for further analysis and characterization. Additionally, enhancement in H_2 yield resulting from CO_2 capture and mineralization is investigated as a function of reaction time and the alkaline sorbent type.

Additional experiments are conducted to determine the exact moles of each gas in the reactor. The experimental set-up is the same as described previously. In this approach, 8 bar of CO is injected into the reactor with 12 bar of N_2. N_2 is used as a reference due to its inert nature and unchanged pressure over the course of the reaction. This approach enables the calculation of the moles for the other gaseous components based on the initial N_2 content. The temperature is increased to a setpoint of 300 °C, and the reaction is performed for 12 hours, while keeping other reaction conditions unchanged, to investigate the influence of Mg- and Ca-bearing hydroxides and silicates on enhancing H_2 conversions.

2.3 Product analysis and characterization

After the reaction, the compositions of effluent gases are analyzed by micro gas chromatography (GC) with the calibration data shown in Fig. S1.† The changes in the composition and structure of the Mg- and Ca-bearing hydroxides and silicates are investigated using infrared (IR) spectroscopy collected in an attenuated total reflection (ATR) mode using an attenuated total reflection-Fourier transform infrared spectrometer (ATR-FTIR, Nicotec™ iS50, Waltham, MA), and X-ray diffractometry (XRD, Bruker D8 Advance ECO powder diffractometer, Bruker), respectively. Furthermore, the morphology and particle sizes are determined using the field emission scanning electron microscope (FESEM, LEO 1550 FESEM, Bruker) and particle size analyzer (Anton Paar). The surface area and the pore size distributions of the sorbents before and after the experiments were determined by N_2 adsorption–desorption isotherms using the Brunauer–Emmett–Teller technique (BET) (Quantachrome Autosorb iQ Analyzer, Boynton Beach, FL) with the BJH model. Prior to measuring the adsorption–desorption isotherms, the samples were outgassed at 140 °C for 12 hours. A ±5% BET instrument error was accounted for all the analysed samples. The concentration of formate in the aqueous phase was measured using a 500 MHz ^1H NMR spectrometer (Bruker AVIII 500) using a solvent suppression method. The calibration line for formate concentration and its corresponding slope, determined using DMSO as internal standards, are shown in Fig. S2.†

3. Results and discussion

3.1 Reaction pathways involved in coupled WGSR with *in situ* CO_2 capture and mineralization for enhanced H_2 conversion

The multiphase reactions involved in coupling the WGSR with *in situ* CO_2 capture and mineralization for enhanced H_2 conversion include: (i) low-temperature conversion of CO and steam over Pt/Al_2O_3 catalyst to produce CO_2 and H_2; (ii) dissolution of Mg- and Ca-bearing hydroxides and silicates to release Mg^{2+} and Ca^{2+} ions, respectively and promote alkalinity; (iii) dissolution of the produced gaseous CO_2 in the alkaline aqueous phase; (iv) reactivity of the hydrated CO_2 with Mg^{2+} and Ca^{2+} ions to mineralize into Mg and Ca-carbonates; and (v) generation of high-purity H_2 due to equilibrium shift due to CO_2 capture and mineralization.

The motivation for using Pt/Al_2O_3 catalyst stems from the need to direct the formation of H_2 as opposed to CH_4.[61] Prior analogous studies showed that Pt or Ni/Al_2O_3 catalysts are effective in reforming aqueous biomass oxygenates such as ethylene glycol and glycerol to produce H_2 and CO_2 preferentially over CH_4.[62] Therefore, in this study, Pt/Al_2O_3 catalysts are used to lower the activation energy barrier, accelerate reaction kinetics, suppress the formation of CH_4, and promote the formation of H_2 and CO_2. Furthermore, the *in situ* capture and conversion of gaseous CO_2 in the presence of alkaline Mg- and Ca-bearing hydroxides and silicates to produce the respective carbonates favors the forward equilibrium shift towards more CO conversion and H_2. Dissolution of Mg – or Ca – bearing hydroxides and silicates releases Mg^{2+} and Ca^{2+} cations which capture and solubilize CO_2 to produce the respective solid carbonates. For example, in this work, the pH of the alkaline slurry is observed to be in the range of 8.69–12.37 for the Mg- and Ca-bearing

580 | *React. Chem. Eng.*, 2025, **10**, 576–592

This journal is © The Royal Society of Chemistry 2025

hydroxides and silicates. This pH is ideal to capture and solubilize CO_2 from the gas phase to produce the respective (bi)carbonate species.

To probe the mechanisms underlying enhanced H_2 conversion by coupling the WGSR with *in situ* CO_2 capture and mineralization, the first set of experiments are conducted by injecting CO gas. Steam required for the WGSR is provided by the slurry. The ratio of CO to steam is calculated and quantified from the steam table (Table S2.1 and 2.2, ESI†). In this approach, the effluent gas compositions are measured using micro gas chromatography (GC), and the molar percentage of each phase is normalized by the total amount of H_2, CO, and CO_2. This approach provides insights into the relative abundance of the gas phase compositions. In this scenario, the relative gas phase composition of H_2 can be elevated if CO_2 is absorbed by the liquid phase, even if CO conversion is unchanged. Therefore, CO conversion is determined for quantifying the enhancement in WGSR using the following expression:

$$R_{CO} = \frac{M\%_{H_2}}{M\%_{H_2} + M\%_{CO}} \quad (3)$$

In this expression, R_{CO} is the conversion of CO, $M\%_{H_2}$, and $M\%_{CO}$ are the mole percentages of H_2 and CO in the measured gas samples, respectively. In this equation, the mole percentage of H_2 is applied as the substitute for the mole percentage of CO_2 because a large amount of generated CO_2 partitions into the aqueous phase as the reactant for carbon mineralization, making it inaccurate to quantify CO_2 only based on the gas phase compositions.

Additionally, the exact number of moles of each gas is necessary to determine the theoretical maximum yield of H_2 and gaseous CO_2 compositions. To this end, additional experiments are conducted with a moderate amount of N_2 in the system as the baseline. In this approach, the absolute number of moles of N_2 is constant throughout the experiment.

This approach enables the determination of the exact moles of H_2, CO, and CO_2 by the van der Waals equation (as shown below) from the normalized mole percentages after the multi-step reactions.
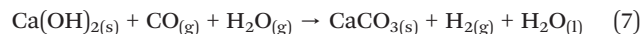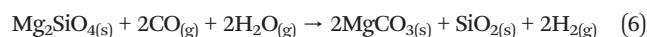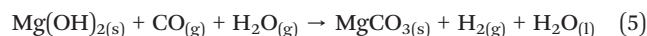
$$\left(P + \frac{n^2 \cdot a}{V^2} \right)(V - n \cdot b) = n \cdot R \cdot T \quad (4)$$

In the expression above, P = pressure, V = volume, a, b = van der Waal's constants, n = number of moles, R = universal gas constant, T = temperature.

3.2 Thermodynamic considerations for enhanced H_2 conversion by coupling the WGSR with *in situ* CO_2 capture and mineralization

The reaction conditions for enhanced H_2 conversion by coupling the WGSR with *in situ* CO_2 capture and mineralization is equilibrium-limited and dictated by the thermodynamics for WGSR to form CO_2 and H_2 and CO_2

capture and mineralization to form Mg- and Ca-carbonates.[48] The detailed reactions associated with coupling the WGSR with *in situ* CO_2 capture and mineralization are below:

$$Mg(OH)_{2(s)} + CO_{(g)} + H_2O_{(g)} \rightarrow MgCO_{3(s)} + H_{2(g)} + H_2O_{(l)} \quad (5)$$

$$Mg_2SiO_{4(s)} + 2CO_{(g)} + 2H_2O_{(g)} \rightarrow 2MgCO_{3(s)} + SiO_{2(s)} + 2H_{2(g)} \quad (6)$$

$$Ca(OH)_{2(s)} + CO_{(g)} + H_2O_{(g)} \rightarrow CaCO_{3(s)} + H_{2(g)} + H_2O_{(l)} \quad (7)$$

$$CaSiO_{3(s)} + CO_{(g)} + H_2O_{(g)} \rightarrow CaCO_{3(s)} + SiO_{2(s)} + H_{2(g)} \quad (8)$$

The overall reaction functions reveal the stoichiometric ratio of the reactants and products, indicating a correlation between equilibrium constants (K_{eq}) and gas species partial pressure (P) at the equilibrium state, respectively:

$$K_{eq}\left(Mg(OH)_2\right) = \frac{P_{H_2}}{P_{CO} \times P_{H_2O}} \quad (9)$$

$$K_{eq}(Mg_2SiO_4) = \frac{P_{H_2}^2}{P_{CO}^2 \times P_{H_2O}^2} \quad (10)$$

$$K_{eq}\left(Ca(OH)_2\right) = \frac{P_{H_2}}{P_{CO} \times P_{H_2O}} \quad (11)$$

$$K_{eq}(CaSiO_3) = \frac{P_{H_2}}{P_{CO} \times P_{H_2O}} \quad (12)$$

The concentration of the different components involved in enhancing H_2 conversion coupled with *in situ* CO_2 capture and mineralization can be determined by their equilibrium constants using thermodynamic properties and relationships as shown by the equation below:[63]
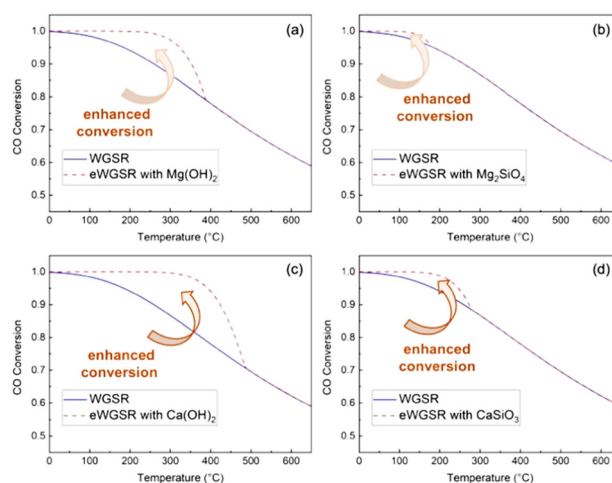

Fig. 3 Enhancement in WGSR as determined from CO conversions based on thermodynamic evaluations in gas–solid reaction mode using (a) $Mg(OH)_2$, (b) Mg_2SiO_4, (c) $Ca(OH)_2$, and (d) $CaSiO_3$ for the *in situ* CO_2 capture. The initial steam-to-CO ratio is 1:1 with adequate sorbents for carbon mineralization. Results for $Mg(OH)_2$ agree with prior studies.[64]

This journal is © The Royal Society of Chemistry 2025

React. Chem. Eng., 2025, **10**, 576–592 | 581

$$K_{eq} = \exp\left(\frac{5693.5}{T} + 1.077 \ln T + 5.44 \times 10^{-4} T - 1.125 \times 10^{-7} T^2 - \frac{49170}{T^2} - 13.148\right) \quad (13)$$

The equilibrium constants determined using expression (13) are used to calculate the theoretical CO conversions as a function of temperature using expressions (9)–(12). Thermodynamic simulations with steam-to-CO ratio of 1:1 are used to determine theoretical CO conversions using $Mg(OH)_2$, Mg_2SiO_4, $Ca(OH)_2$, and $CaSiO_3$ as alkaline sources (Fig. 3).

Notably, the WGSR and enhanced WGSR (or eWGSR) conversions define the theoretical percentage of CO converted to CO_2 at the equilibrium. CO_2 conversions are calculated from the partial pressure of H_2, CO, and steam. The theoretical CO conversion of $Mg(OH)_2$ confirms prior reported calculations.[64] CO conversions at equilibrium decrease with increasing temperature due to the exothermic nature of the reactions (Fig. 3). Compared with conventional WGSR, a significant enhancement in CO conversion is noted at temperatures below 350 °C, indicating that Mg- and Ca-bearing hydroxides and silicates are effective in aiding CO (and H_2) conversion by capturing CO_2. It is interesting to note that at temperatures below 350 °C, $Mg(OH)_2$ and $Ca(OH)_2$ enhance CO conversion at 250 °C and 300 °C due to in situ capture of gaseous CO_2.

In contrast, the enhancement in CO conversion realized using Mg- and Ca-bearing silicates is achieved below 200 °C. Based on these thermodynamic analyses, it is evident that CO conversion can be enhanced using Ca- and Mg-bearing silicates in gas–solid reaction modes. To overcome the mass transfer limitations associated with gas–solid reactions, multiphase gas–liquid–solid reactions are proposed to accelerate the kinetics of WGSR when coupled with aqueous CO_2 capture and mineralization pathways at temperatures below 300 °C. These experimental conditions are a significant departure from conventional sorbent-enhanced WGSR operating in a gas–solid mode to capture CO_2.

3.3 Enhancement in WGSR using $Mg(OH)_2$ and Mg_2SiO_4

To enhance H_2 conversion with in situ CO_2 capture, it is essential to use a suitable catalyst that will convert CO and steam to produce H_2 and CO_2 and an alkaline source to capture CO_2.[65] Prior studies have reported enhancement in H_2 conversion via sorbent – enhanced WGSR using Ca-bearing sorbents.[46] Enhancement in H_2 yields were also reported by coupling the WGSR with slurry phase CO_2 capture and mineralization using $Mg(OH)_2$.[66] However, $Mg(OH)_2$ needs to be directly mined or extracted from earth – abundant Mg-silicates. Eliminating this additional mining or extraction step and directly using earth – abundant Mg-silicate minerals for enhancing H_2 conversion while capturing CO_2 is less explored but highly transformative. To address this knowledge gap, experiments are conducted to contrast the influence of $Mg(OH)_2$ vs. Mg_2SiO_4 on enhancing

H_2 yield with in situ CO_2 capture. The abundance of olivine $(Mg,Fe)_2SiO_4$ bearing forsterite (Mg_2SiO_4) in the natural environment motivates the direct use of these materials for CO_2 capture.[39] To investigate the enhancement in H_2 yield with CO_2 capture, the gaseous products at the effluent are analyzed. Following this, the structures and morphologies of the carbonate-bearing products are characterized separately.

Initially, a blank experiment is performed by considering only the WGSR over Pt/Al_2O_3 catalyst, to investigate its catalytic activity in the low-temperature regime. Fig. 4(a) represents the gas mole percentages when feeding only 20 bar CO at 250 °C for 9 hours. Fig. 4(b) shows the conversion of CO for the blank experiment and the cases with $Mg(OH)_2$ and Mg_2SiO_4. In the absence of the alkaline resource, CO conversion of 72.4% is noted (Fig. 4(b)). Gas analyses did not indicate any CH_4 formation demonstrating that the Pt/Al_2O_3 catalyst is effective in converting CO and steam to CO_2 and H_2. The observed higher selectivity towards H_2 using low-temperature Pt/Al_2O_3 catalyst is consistent with previous literature on WGSR.[27] Compared with the blank experiment without any alkaline source, WGSR reactions in the presence of a slurry bearing $Mg(OH)_2$ or Mg_2SiO_4 enhanced CO conversion and H_2 yield and lowered the concentration of gaseous CO_2 due to in situ CO_2 capture. In contrast to the blank experiment without the alkaline source, CO conversions in the presence of $Mg(OH)_2$ and Mg_2SiO_4 at 250 °C are 81% and 79.7%, respectively, as seen in Fig. 4(b). The molar compositions of H_2 and CO_2 in the gas phase are 50.8% and 30.3% for H_2 and CO_2 for the blank experiment. In contrast, H_2 concentrations increase by 18% and 9.5%, and CO_2 concentrations decrease by 15.9% and 6.1% in the presence of $Mg(OH)_2$ and Mg_2SiO_4 compared to the blank experiment (Fig. 4(a)).

The relative composition of H_2 in the gas phase is 8.6% higher when $Mg(OH)_2$ is used for CO_2 capture as opposed to Mg_2SiO_4. CO_2 concentrations are nearly 10% lower when $Mg(OH)_2$ is used as opposed to Mg_2SiO_4. Higher H_2 concentrations and lower CO_2 concentrations in the presence of $Mg(OH)_2$ versus Mg_2SiO_4 are attributed to the faster dissolution kinetics of $Mg(OH)_2$ relative to Mg_2SiO_4.[67] The enhanced release of Mg^{2+} ions favors CO_2 capture and the forward WGSR reaction which results in enhanced H_2 conversions and CO consumption (Fig. 4(a) and (b)).

3.4 Enhancement in H_2 conversion with in situ CO_2 capture as a function of time using $Mg(OH)_2$ and Mg_2SiO_4 materials

One of the key uncertainties in enhancing H_2 conversions with in situ CO_2 capture is the influence of the reactivity of the alkaline resources in hydrothermal environments. In this context, even though it is known that $Mg(OH)_2$ is

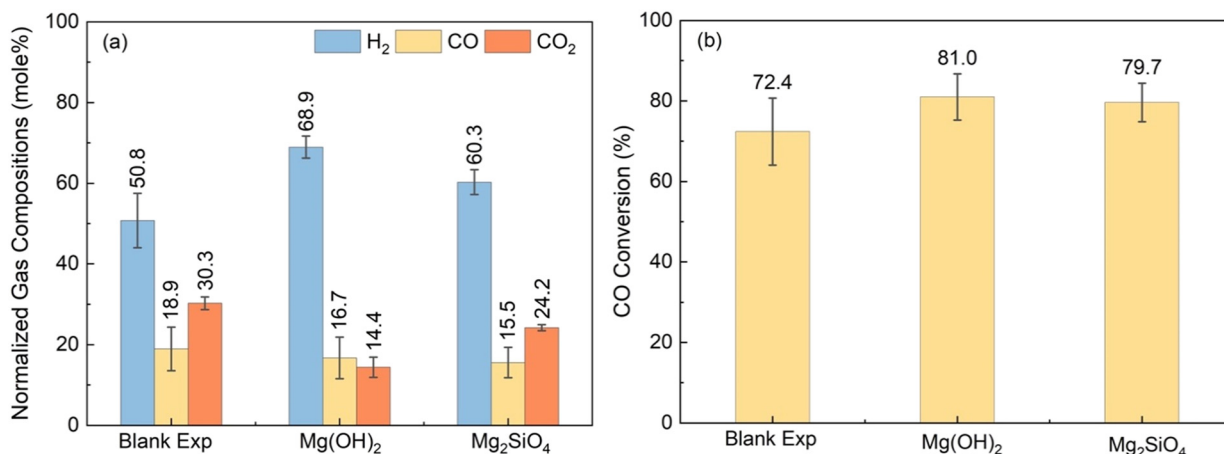582 | React. Chem. Eng., 2025, 10, 576–592

This journal is © The Royal Society of Chemistry 2025

Fig. 4 Contrasting the influence of $Mg(OH)_2$ and Mg_2SiO_4 on the water gas shift reaction (WGSR) as determined from H_2, CO, and CO_2 compositions in (a) and CO conversions in (b). Experiments are conducted at 250 °C, 20 atm for 9 h. The blank experiment is conducted over 3 g of Pt/Al_2O_3 catalyst without alkaline source. The $Mg(OH)_2$ and Mg_2SiO_4 cases are conducted over 3 g of Pt/Al_2O_3 catalyst with a sorbent-to-liquid weight ratio of 3 : 10, leading to mole percentages of 8.48% for $Mg(OH)_2$ and 3.70% for Mg_2SiO_4, respectively.

more soluble and has faster kinetics of dissolution compared to Mg_2SiO_4, the kinetics associated with accelerating WSGR are not well understood. Several factors could be competing in this integrated and enhanced WGSR approach.

First, the gas phase conversion of CO and steam to H_2 and CO_2 can be limiting. Second, the solubility of CO_2 and reactivity of Ca- and Mg-bearing silicates and hydroxide to capture CO_2 can be slow. Based on the changes in the compositions of the gas phase over time, the factors limiting the conversion of CO and H_2O to H_2 with *in situ* CO_2 capture can be determined. To this end, experiments are conducted with $Mg(OH)_2$ and Mg_2SiO_4 at 250 °C, 20 atm as a function of reaction time. The normalized gas phase compositions for reactions conducted at 3, 6, 9, and 12 hours are shown in Fig. 5(a) and (b) in the presence of $Mg(OH)_2$ and Mg_2SiO_4, respectively.

In the first three hours of the reaction with $Mg(OH)_2$ as the alkaline source, H_2 composition is 53.4% while that of CO and CO_2 are 18.7 and 27.9%, respectively. An increase in H_2 composition to 68.9% and a decrease in CO and CO_2 compositions to 16.7% and 14.4%, respectively are noted in the 9-hour cases. These results indicate that $Mg(OH)_2$ is effectively enhancing CO conversions and H_2 yields with inherent CO_2 capture. Therefore, the WGSR is not the limiting factor in H_2 conversion in the first nine hours of the reaction. However, increasing the reaction time from 9 hours to 12 hours, lowered H_2 compositions from 68.9% to 60.9%. CO and CO_2 compositions increased from 16.7 to 23.4% and 14.4 to 15.8%, respectively, when the reaction time is increased from 9 hours to 12 hours. These results suggest that CO_2 capture is the likely limiting factor as the reaction time increases from 9 to 12 hours. This observation can be attributed to the fact that at increased reaction times, the
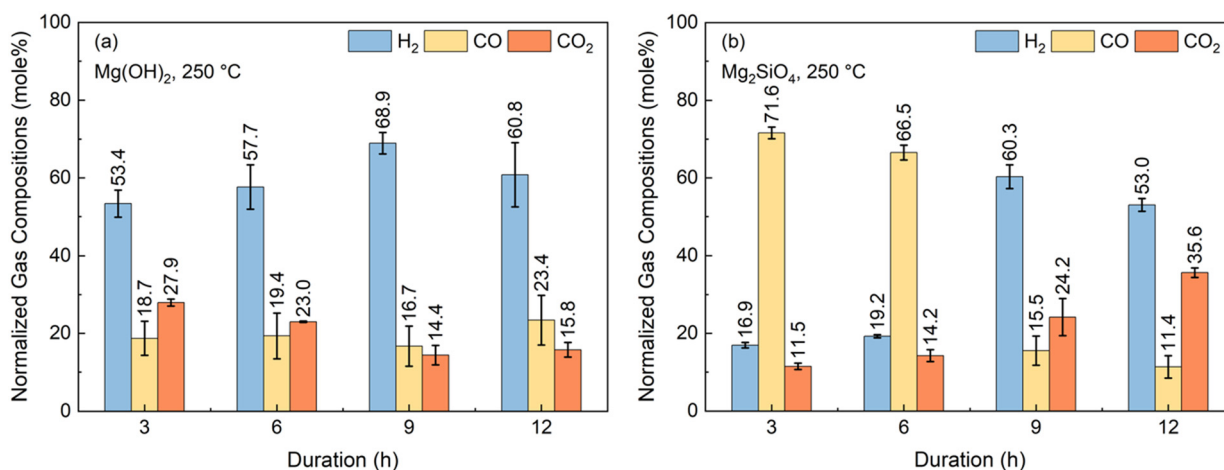

Fig. 5 Determination of time dependence on the concentrations of H_2, CO, and CO_2 when the WGSR is coupled with *in situ* CO_2 capture and mineralization using (a) $Mg(OH)_2$ and (b) Mg_2SiO_4. The $Mg(OH)_2$ and Mg_2SiO_4 cases are conducted at 250 °C and 20 atm over 3 g of Pt/Al_2O_3 catalyst with a sorbent-to-liquid weight ratio of 3 : 10, leading to mole percentages of 8.48% for $Mg(OH)_2$ and 3.70% for Mg_2SiO_4, respectively.

This journal is © The Royal Society of Chemistry 2025

React. Chem. Eng., 2025, **10**, 576–592 | **583**

availability of Mg^{2+} ions for CO_2 capture is likely decreasing over time. Slower dissolution rates of $Mg(OH)_2$ over time due to mass transfer arising from the formation of Mg-carbonates[68] or due to the saturation of the solution with Mg^{2+} ions are attributed to the decrease in H_2 and increase CO_2 compositions at 12 hours.

In contrast, Mg_2SiO_4 for *in situ* CO_2 capture yielded significantly different results compared to the use of $Mg(OH)_2$ (Fig. 5(b)). H_2 compositions are 16.9% and 19.2% respectively, at 3 hours and 6 hours of reaction time, while CO compositions are 71.6% and 66.5% in the presence of Mg_2SiO_4. These results indicate that the WGSR is the limiting step in the first 6 hours of reaction in the presence of Mg_2SiO_4. This is likely due to the slower dissolution behavior of Mg_2SiO_4 to release Mg^{2+} ions compared to that of $Mg(OH)_2$. As a result, *in situ* CO_2 capture and subsequent enhancement in H_2 yields is limited in the presence of Mg_2SiO_4 in the first six hours of the reaction. At 9 hours of reaction time, H_2 composition is 60.3%. CO composition of 66.5% at 6 hours decrease to 15.5% at 9 hours of reaction time (Fig. 5(b)). These results indicate that while the kinetics of WGSR are slower in the first 6 hours of the reaction in the presence of Mg_2SiO_4 compared to in the presence of $Mg(OH)_2$, comparable compositions are achieved when the reaction time is 9 hours.

As in the case of Mg_2SiO_4, a decrease in H_2 compositions and increase in CO_2 compositions is observed when the reaction time is 12 hours. H_2 compositions decrease from 60.3% to 53.0% while CO_2 compositions increase from 24.2% to 35.6% at 12 hours of reaction. The relative decrease in H_2 compositions and increase in CO_2 compositions at 12 hours is attributed to the mass transfer limitations associated with the dissolution of Mg- silicate and Mg-hydroxide. Therefore, these studies indicate that WGSR can be the initial slow step in the presence of Mg_2SiO_4 as opposed to $Mg(OH)_2$ during

the first 6 hours of reaction. Non-monotonic changes in the concentrations of H_2, CO, and CO_2 observed as the reaction time increases from 9 hours to 12 hours are likely due to limitations from the slow dissolution of $Mg(OH)_2$ and Mg_2SiO_4 to release Mg^{2+} ions for CO_2 capture.

3.5 Influence of Mg- and Ca-bearing hydroxides and silicates on enhanced H_2 conversion with *in situ* CO_2 capture

Contrasting the influence of Mg- and Ca-bearing silicates and hydroxides on enhanced H_2 conversion coupled with *in situ* CO_2 capture can unlock new opportunities for the utilization of a wide range of alkaline feedstocks. Ca-bearing hydroxides and silicates are abundant in fly ash and slags.[69] Mg-bearing hydroxides and silicates are abundant in ultramafic and mafic mine tailings.[70] To this end, experiments are conducted at 300 °C in the presence of 8 bar of CO and 12 bar of N_2 in the gas phase and $Mg(OH)_2$, $Ca(OH)_2$, Mg_2SiO_4, or $CaSiO_3$ to capture CO_2 in a slurry phase over a reaction time of 12 hours, as noted in section 3.1. Pt/Al_2O_3 catalyst is used as a low-temperature WGSR catalyst. N_2 gas is used as a reference due to its inert nature and constant quantity before and after the reaction which enables the determination of the moles of gas products formed. The influence of $Mg(OH)_2$, $Ca(OH)_2$, Mg_2SiO_4, or $CaSiO_3$ on compositions of H_2, CO, and CO_2 are shown in Fig. 6.

The influence of WGSR alone in the absence of Ca- and Mg-bearing hydroxide and silicate determined at the same experimental conditions as the others showed that H_2, CO, and CO_2 account for 41.85%, 33.76%, and 24.39%, respectively (Fig. 6(a)). Relative to this blank experiment, the highest enhancement in H_2 conversion and CO_2 suppression was observed in the presence of $Ca(OH)_2$. In this best case scenario with $Ca(OH)_2$, H_2 yield is 72.67% which is 30.82% higher compared to the blank experiment. CO_2 yields are

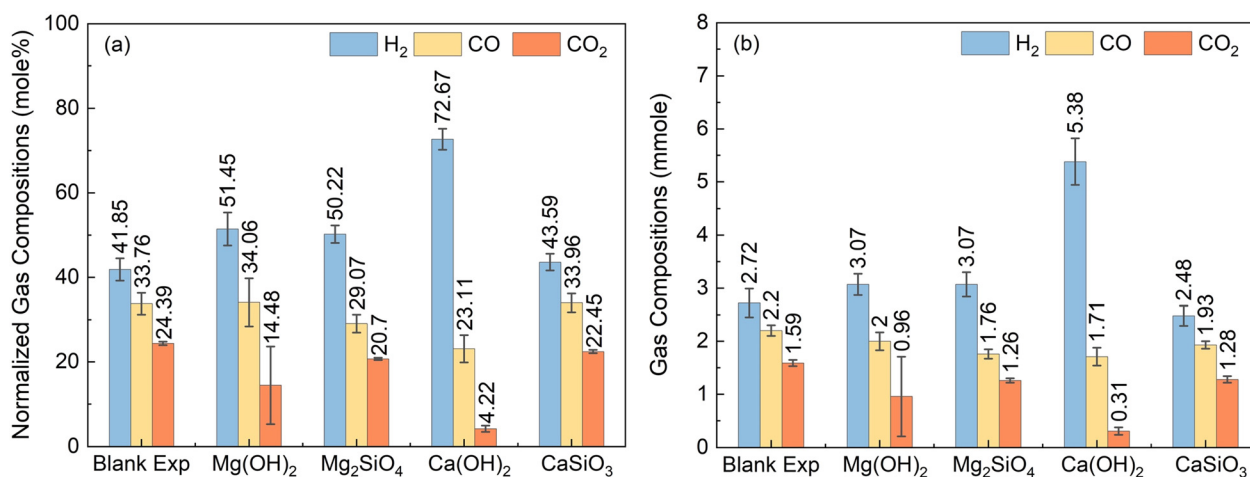**Fig. 6** Contrasting the influence of alkaline resources such as $Mg(OH)_2$, Mg_2SiO_4, $Ca(OH)_2$, and $CaSiO_3$ on enhancing H_2 yield with *in situ* CO_2 capture and mineralization where (a) represents normalized gas mole percentages and (b) represents exact gas moles. Experiments are conducted at 300 °C, 20 atm for 12 h. The blank experiment is conducted over 3 g of Pt/Al_2O_3 catalyst without any alkaline source. The test experiments are conducted over 3 g of Pt/Al_2O_3 catalyst with a sorbent-to-liquid weight ratio of 3:10, leading to mole percentages of 8.48% for $Mg(OH)_2$, 3.70% for Mg_2SiO_4, 6.80% for $Ca(OH)_2$, and 4.45% for $CaSiO_3$, respectively.

584 | *React. Chem. Eng.*, 2025, **10**, 576–592

This journal is © The Royal Society of Chemistry 2025

suppressed by 20.17% to 4.22% relative to the blank experiment indicating that $Ca(OH)_2$ in the slurry is highly effective in capturing CO_2 emissions. Significant enhancement in WGSR is also evident from the changes in CO compositions which are lowered by 10.65% compared to the blank experiment. In comparison to $Ca(OH)_2$, the H_2 yields are ~50–51% in the presence of $Mg(OH)_2$ and Mg_2SiO_4 which are lower. Interestingly, CO compositions are 5% lower when Mg_2SiO_4 is used compared to $Mg(OH)_2$, indicating WGSR is enhanced in the presence of Mg_2SiO_4. However, the higher solubility of $Mg(OH)_2$ compared to Mg_2SiO_4 enhances CO_2 capture lowering CO_2 compositions by 6.22% when $Mg(OH)_2$ is used related to Mg_2SiO_4.[67]

The reactivity of $CaSiO_3$ in enhancing H_2 yield and suppressing CO_2 emissions is lower compared to the other alkaline sources. Compared to the blank experiment, the composition of H_2 is 1.74% higher, CO is similar, and CO_2 is ~2% lower. While these results indicate that $CaSiO_3$ enhances H_2 conversion and enables CO_2 capture, substantial changes relative to the blank experiment are not observed. The composition data in mmoles are reported in Fig. 6(b) for use in subsequent modeling efforts. The results reported in Fig. 6 indicate that the effectiveness of the alkaline sources in enhancing H_2 yields while capturing CO_2 emissions follows this order: $CaSiO_3 < Mg_2SiO_4 < Mg(OH)_2 < Ca(OH)_2$. As hypothesized, the reactivity of Ca- and Mg-bearing hydroxides in enhancing H_2 yield and suppressing CO_2 emissions is higher compared to that of the corresponding silicates. The higher solubility and faster dissolution rates of Ca- and Mg-bearing hydroxides compared to the corresponding silicates facilities enhanced CO_2 capture and H_2 conversion.[67]

3.6 Mechanistic insights underlying enhancement in H_2 conversion coupled with *in situ* CO_2 capture and mineralization

The key reasons for the differences in the reactivity of Ca- and Mg-bearing silicates *vs.* hydroxides are the slower kinetics of dissolution of silicates and the formation of a

silica passivation layer which is known to limit mass transfer.[71,72] Fig. 7 represents the multiphase chemical reaction mechanisms associated with carbon mineralization by harnessing hydroxides *versus* silicates. While the CO_2 hydration reactions to produce bicarbonate and carbonate species remain unchanged, the leaching of the metal into the solution results in the formation of a silica-rich layer in the case of silicates unlike in hydroxides. It is interesting to note that despite the slower kinetics of Mg-silicate dissolution and the formation of a silica layer that can limit mass transfer, comparable gas phase compositions of H_2, CO, and CO_2 are noted with $Mg(OH)_2$ and Mg_2SiO_4 (Fig. 6). However, the kinetics associated with enhancing H_2 conversion with *in situ* CO_2 capture and mineralization can differ significantly as noted in Fig. 5. The slow kinetics of WGSR observed up to 6 hours in the presence of Mg_2SiO_4 are attributed to limited availability of Mg^{2+} ions to capture CO_2 and facilitate the forward reaction. However, beyond 6 hours of reaction time, the observed enhancement in H_2 yields and corresponding decrease in CO_2 emissions is attributed to the availability of sufficient Mg^{2+} ions to capture CO_2 and aid the forward WGSR to produce H_2.

Prior studies have shown that temperatures above 100 °C and high partial pressures of CO_2 aid the carbon mineralization of olivine.[39,73] The solubility of CO_2, and dissolution of Mg_2SiO_4 to release Mg^{2+} ions for capturing CO_2 and producing carbonates at the experimental conditions used in this study are analogous to those reported in prior studies. Therefore, despite the slow initial kinetics of Mg_2SiO_4, the release of Mg^{2+} ions over time results in comparable H_2, CO, and CO_2 compositions as when $Mg(OH)_2$ is used. It is also interesting to note that Mg_2SiO_4 is more effective in enhancing WGSR compared to $CaSiO_3$. Prior studies reported that $CaSiO_3$ is reactive at temperatures as low as 110 °C for carbon mineralization, unlike Mg_2SiO_4.[74] Possible reasons for the lower-than-expected reactivity of $CaSiO_3$ are the formation of a silica passivation layer that is thicker and limits mass transfer at the experimental conditions reported in this study. To uncover if CO_2 uptake by the alkaline slurry results in the formation of solid carbonates, detailed structural and morphological analyses are investigated and reported in the following section.

3.7 Structural and morphological analyses of the alkaline sources

To determine if the captured CO_2 only dissolves in the aqueous phase or reacts to produce solid carbonates, the changes in the structural and morphological features of the alkaline resources are determined. The crystalline features in unreacted and reacted Ca- and Mg-bearing silicates and hydroxides using X-ray diffraction (XRD) measurements (Fig. 8). As shown in Fig. 8(a), the unreacted $Mg(OH)_2$ exhibits the typical diffractogram of hexagonal $Mg(OH)_2$ brucite structure with characteristic XRD peaks at 33.2°, 38.1°, 50.6°, 58.7°, 68.3°, and 72.1° (see peaks in black).
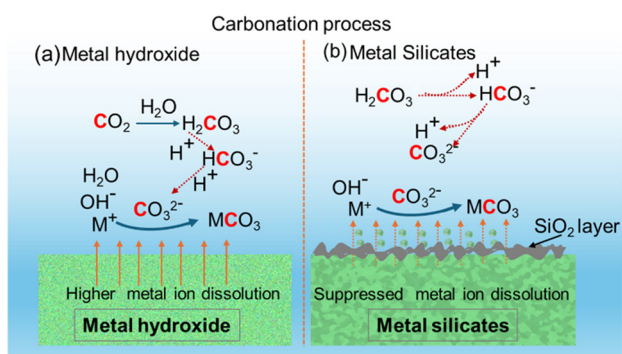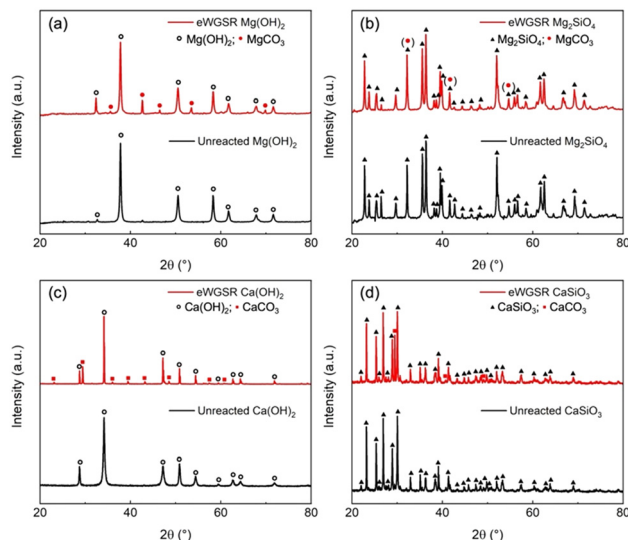

Fig. 7 Schematic diagram of surface reactions, dissolution, and mineralization process over (a) metal hydroxides and (b) metal silicates sorbents.

This journal is © The Royal Society of Chemistry 2025

React. Chem. Eng., 2025, **10**, 576–592 | 585

Fig. 8 Determination of the crystalline phases before and after reaction starting with (a) $Mg(OH)_2$, (b) Mg_2SiO_4, (c) $Ca(OH)_2$, and (d) $CaSiO_3$ using X-ray diffraction (XRD) analyses.

These peaks are well in accordance with the reported literature (PDF 44-1482).[75] The diffractogram of the reacted solid (peak in red) revealed the existence of magnesite ($MgCO_3$) peaks along with suppression of $Mg(OH)_2$ intensities. This co-existence indicates the dissolution of $Mg(OH)_2$ and the capture and conversion of CO_2 to produce $MgCO_3$.[73] To investigate if $MgCO_3$ is formed starting from Mg_2SiO_4 precursors, XRD data of the unreacted and reacted materials are collected and shown in Fig. 8(b). The X-ray diffraction pattern corresponding to the monoclinic structure of unreacted Mg_2SiO_4 is shown in Fig. 8(b).

The reacted Mg_2SiO_4 product exhibits a very similar scattering pattern as the unreacted material, which can results from overlapping between (104) peak of the generated magnesite and (130) peak of the residual Mg_2SiO_4.[76,77] To further distinguish the different phases and prove the formation of carbonate, additional characterization is required. Interestingly, the absence of the nesquehonite ($MgCO_3 \cdot 3H_2O$) or hydromagnesite ($Mg_5(CO_3)_4(OH)_2 \cdot 4H_2O$) phases in our case is due to the higher stability of anhydrous magnesite ($MgCO_3$) at elevated temperatures and pressures.[39] Additionally, the formation of Mg-carbonate can be influenced by numerous other factors, including the reaction time, ionic strength or the addition of reagents including salts.[39] Thus, in this study, the formation of anhydrous magnesite ($MgCO_3$) can be attributed to the application of high temperatures of 250–300 °C with elevated CO_2 partial pressures in the range of 10–20 atm for reaction durations of 9–12 hours.

The structural arrangement characterization of the Ca cases shows a similar trend with Mg cases, in which the anhydrous calcite ($CaCO_3$) is the unique carbonate product due to the favorable reaction conditions. Fig. 8(c) illustrates the XRD peaks of unreacted $Ca(OH)_2$ at 28.7°, 34.1°, 47.2°,

50.6°, 54.3°, 62.3°, and 64.3° corresponds to the (100), (101), (102) (110), (111), (201) and (112) planes, respectively. Several studies have reported similar patterns of $Ca(OH)_2$.[78,79] After the enhanced WGSR, the reacted product shows the presence of both $Ca(OH)_2$ and $CaCO_3$ phases (JCPDS 84-1276 and 85-1108, respectively). The occurrence of peaks at 23.1°, 29.5°, 31.6°, 36.1°, 39.5°, 43.3°, 47.2°, 47.6°, 48.6°, 57.5°, 61.1°, and 64.5° corresponds to (012), (104), (006), (110), (114), (202), (024), (018), (116), (112) (119), and (300) planes, respectively. These XRD patterns corresponded to the rhombohedral crystal structure of $CaCO_3$.[80] Furthermore, Fig. 8(d) shows the diffraction peaks of unreacted sorbents can be indexed as the $CaSiO_3$.[81] For the reacted $CaSiO_3$, the XRD peaks resemble the co-occurrence of $CaSiO_3$ and $CaCO_3$ phases, which is a low-temperature polymorph of calcium carbonate (JCPDS 00-005-0586).[82]

Furthermore, the morphologies of the reacted $Mg(OH)_2$, $Ca(OH)_2$, Mg_2SiO_4, and $CaSiO_3$ materials are determined using FE-SEM to identify carbonate-bearing phases. Fig. 9(b) shows the cube-like structure of $MgCO_3$ with the appearance of residual $Mg(OH)_2$ after carbon mineralization, confirming the carbonate formation after the enhanced WGSR. Similarly,
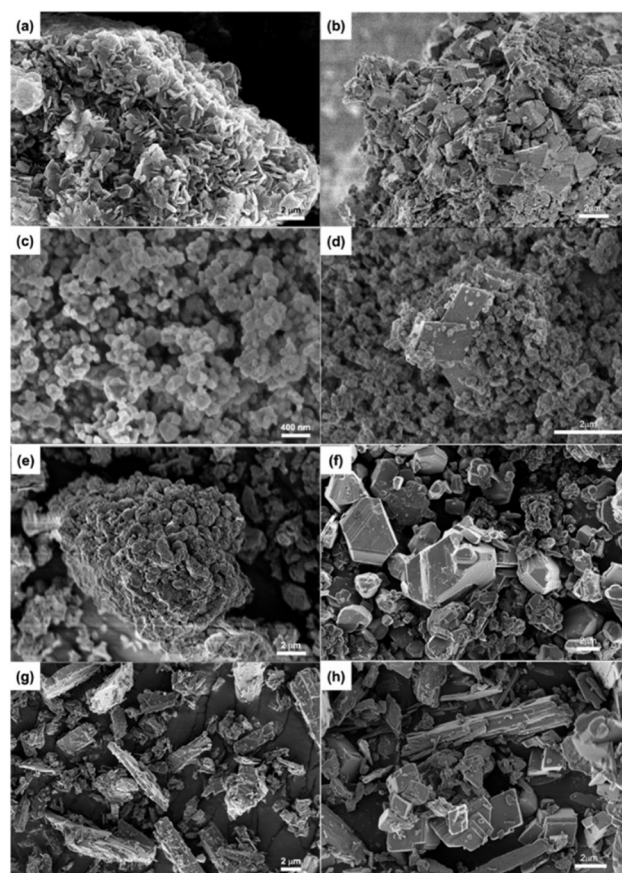
Fig. 9 Morphology of (a) unreacted $Mg(OH)_2$; (b) reacted $Mg(OH)_2$; (c) unreacted Mg_2SiO_4; (d) reacted Mg_2SiO_4; (e) unreacted $Ca(OH)_2$; (f) reacted $Ca(OH)_2$; (g) unreacted $CaSiO_3$; (h) reacted $CaSiO_3$ determined by scanning electron microscope measurements.

586 | *React. Chem. Eng.*, 2025, **10**, 576–592

This journal is © The Royal Society of Chemistry 2025

Table 2 The surface area, pore volume, and mean pore diameter of the unreacted and reacted alkaline sources as determined using BET analyses and the BJH method

|	Unreacted alkaline sources			Reacted alkaline sources		
	Surface area ($m^2 \ g^{-1}$)	Pore volume ($cm^3 \ g^{-1}$)	Mean pore diameter (nm)	Surface area ($m^2 \ g^{-1}$)	Pore volume ($cm^3 \ g^{-1}$)	Mean pore diameter (nm)
$Mg(OH)_2$	9.78	0.047	4.01	6.48	0.05	3.93
Mg_2SiO_4	17.41	0.050	2.81	14.93	0.08	3.93
$Ca(OH)_2$	24.29	0.107	3.72	4.81	0.01	1.50
$CaSiO_3$	5.00	0.020	2.66	6.20	0.02	3.94

the cube-shaped $MgCO_3$ particles emerged in the case of reacted Mg_2SiO_4 materials (Fig. 9(d)).

Interestingly, the granular particles covered on cubic $MgCO_3$ particles can be attributed to the residual Mg_2SiO_4 and associated SiO_2 layer resulting from silicate dissolution. Similar phenomena are also observed in the reacted $Ca(OH)_2$ and $CaSiO_3$ materials (Fig. 9(f) and (h)). Additionally, the large hexagonal particles indicate the significant dissolution and recrystallization of initial $Ca(OH)_2$ sorbents (Fig. 9(f)), and the elongated particles correspond to the residual $CaSiO_3$ materials (Fig. 9(g) and (h)). Interestingly, the XRD analysis does not show the clear existence of crystalline phases rich in silica, indicating the potential presence of an amorphous silica-rich layer or glassy SiO_2 coating that may cause the suppression in metal dissolution in $CaSiO_3$, Mg_2SiO_4, responsible for the low extents of carbon mineralization.

As a further clarification of the sorbents' morphological evolution, the surface area and the pore distribution determined by BET analysis are listed in Table 2. The decreased surface area in $Mg(OH)_2$, Mg_2SiO_4, and $Ca(OH)_2$ cases indicates the formation of larger carbonate particles like $MgCO_3$ and $CaCO_3$ (Fig. 9(a)–(f)). Notably, the significant surface area reduction in the $Ca(OH)_2$ case aligns with its more effective CO_2 mineralization and the corresponding greater carbonate formation. In contrast, due to the larger particle size and limited pore volume in the unreacted $CaSiO_3$ compared with the generated $CaCO_3$, the small increase in the surface area and pore volume after reaction are attributed to the dominance of dissolution over carbon mineralization (Fig. 9(g) and (h)). Furthermore, the pore size distributions determined using the BJH model are illustrated in Fig. S4.† The unreacted hydroxide sorbents exhibit relatively narrow pore distributions, centered at approximately 4.01 nm for $Mg(OH)_2$ and 3.72 nm for $Ca(OH)_2$. Post-reaction, significant pore structure rearrangements are observed, leading to reductions in both pore volume and diameter, particularly for $Ca(OH)_2$. Additionally, the formation of $MgCO_3$ results in more well-ordered pore and particle size distributions compared to the Mg_2SiO_4 precursor. Conversely, significant changes in the pore size distribution of $CaSiO_3$ before and after reaction are not observed due to the relatively low extent of carbon mineralization.

Attenuated total reflection Fourier transform infrared (ATR-FTIR) analysis is also performed on unreacted sorbents

and reacted products to confirm carbonate formation after the enhanced WGSR. As shown in Fig. 10(a) and (c), unreacted hydroxide sorbents exhibited only one peak between 3600–3700 cm^{-1}, indicating the purity of starting materials ($Mg(OH)_2$, $Ca(OH)_2$).[83] On the other hand, the occurrence of new peaks around 1400–1500 cm^{-1}, 850–890 cm^{-1}, and 700–750 cm^{-1} corresponds to C–O asymmetric stretching vibrations, the C–O bending vibration, and the in-plane bending vibration of O–C–O, respectively, in the carbonated products formed after the enhanced WGSR.[84,85] Furthermore, peaks shown in ATR-FTIR of unreacted Mg_2SiO_4 sorbents around 600–650 cm^{-1} are consistent with SiO_4 bending and stretching modes, respectively, while the peak around 1000 cm^{-1} represents asymmetric stretching modes of Si–O–Si.[86,87] As shown in Fig. 10(b), despite its very low intensity, the peak at 1100 cm^{-1} could be interpreted as a symmetric C–O stretching vibration band indicating the carbon mineralization of Mg_2SiO_4.[84] Moreover, in the case of $CaSiO_3$ materials, the presence of peaks approximately 600–700 cm^{-1}, 900 cm^{-1} corresponds to the symmetrical stretching of O–Si–O bonds and Si–O–Ca bonds, while the peaks between 1000–1100 cm^{-1} correspond to a symmetrical stretching of Si–O–Si bonds, respectively.[88] As shown in Fig. 10(d), the typical peaks from silicate remained constant
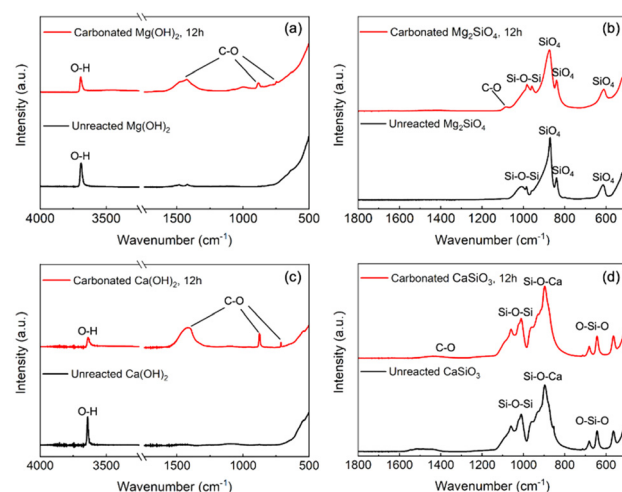
Fig. 10 Identification of different functional groups using attenuated total reflection-Fourier transform infrared (ATR-FTIR) spectroscopy measurements in unreacted and reacted (a) $Mg(OH)_2$; (b) Mg_2SiO_4; (c) $Ca(OH)_2$; (d) $CaSiO_3$ materials.

after the enhanced WGSR with a little shoulder around 1400 cm^{-1}, indicating the asymmetric stretching mode of C–O, proving the carbon mineralization of CaSiO$_3$ material.[85]

Further, to investigate the effect of eWGSR on the metal hydroxides and metal silicates, XPS analyses are conducted. The XPS spectra were calibrated based on the carbon C–C peak (284.8 eV).[89] Fig. S5(a1) and (a2)† shows the O 1s deconvolution result for unreacted and reacted Mg(OH)$_2$ materials. The high-resolution XPS spectrum of unreacted Mg (OH)$_2$ exhibit a peak at binding energy of 531.7 eV which suggests the existence of hydroxyl (OH) species. Furthermore, the reacted Mg(OH)$_2$ materials showed slight changes in O 1s spectrum (Fig. S5(a2)†). Binding energy (BE) peaks are observed at 531.8 eV and 533.34 eV which correspond to hydroxyl (OH) and carbonate (CO$_3^{2-}$) species, respectively.[90,91] Similar trends are observed within the unreacted and reacted Ca(OH)$_2$ materials. The hydroxyl (OH) peak at 531.9 eV exclusively appears in the unreacted Ca(OH)$_2$ while the hydroxyl peak at 531.8 eV and carbonate peak at 532.9 co-exists in the reacted Ca(OH)$_2$ material (Fig. S5(b1) and (b2)†). To further determine the influence of enhanced WGSR on metal silicates (CaSiO$_3$ and Mg$_2$SiO$_4$), the valance state of the oxygen in the unreacted and reacted silicates are studied using XPS analyses. Fig. S6† shows the carbon (C1s) spectra from unreacted and reacted Mg$_2$SiO$_4$, CaSiO$_3$ materials consisting of two main components arising from C–C (~284.4 eV) and O=C (carboxyl, ~288.6 eV).[92,93] Compared to unreacted counterparts, the reacted materials exhibit higher intensity signal of C 1s indicating the presence of carbonate (CO$_3^{2-}$) species. The C 1s peak values observed between 289.5 eV and 289.7 eV are well-matched with the carbonate (CO$_3^{2-}$) species in the reported literature.[94,95]

Insights into the changes in the structure of silicon are obtained from XPS analyses. Fig. S7(a1)† shows that O 1s peak at 531.35 eV corresponds to the SiO$_4$ tetrahedra in the unreacted Mg$_2$SiO$_4$.[96] Additionally, the O1s peak tail at a higher binding energy region around 533.6 eV could result from minor amorphous SiO$_2$ content.[97] On the other hand, the reacted Mg$_2$SiO$_4$ materials ((Fig. S7(a2)†) show deconvoluted peaks at 531.1, 532.3, and 533.5 eV which corresponds to the residual Mg$_2$SiO$_4$, the generated carbonate and the amorphous SiO$_2$ resulting from silicate dissolution.[98–101] On the contrary, Fig. S7(b1)† shows that unreacted CaSiO$_3$ exhibits a SiO$_2$ peak at 533.5 eV other than the typical SiO$_3$ peak at 532 eV, indicating the presence of an amorphous phase in the unreacted sorbent.[97,102] After the enhanced WGSR, the O1s peaks of the reacted CaSiO$_3$ shift towards a high binding energy range. More specifically, the existence of deconvoluted O1s peaks at 531.4 eV, 532.9 eV, and 533.3 eV correspond to the residual SiO$_3$, generated carbonate and SiO$_2$, which confirms carbonate formation and the dissolution of calcium silicate material.
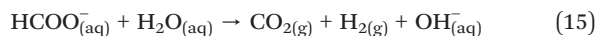
Further, Fig. S7(c1) and (d1)† depicts the existence of Si2p broad peak at the binding energy of 102.7 eV and 103.2 eV for unreacted Mg$_2$SiO$_4$ and CaSiO$_3$, respectively.[103] It's worth noting that the SiO$_2$ peaks around 104 eV appear in both the

silicates, corresponding to the results from O1s peak.[104] However, after carbon mineralization, Si 2p deconvoluted spectra shows the diminished SiO$_4$ or SiO$_3$ peaks with intensified SiO$_2$ peaks for both silicates, indicating the dissolution of silicate and the generation of Si-rich passivation layer.[105,106] Additionally, the relatively high amorphous SiO$_2$ component in the unreacted CaSiO$_3$ compared to Mg$_2$SiO$_4$ likely suppresses the dissolution of CaSiO$_3$, thus resulting in lowering H$_2$ yields compared to Mg$_2$SiO$_4$ materials.

To quantitatively evaluate the carbonate phases, the carbon/metal ratios are calculated before and after the enhanced WGSR based on the atom% from XPS (Fig. S8†). The detected carbon phase in the unreacted carbonate-free sorbents can be attributed to the adventitious carbon on samples' surface due to the carbon contamination during air exposure.[107] However, neglecting the impact from adventitious carbon, the carbon/metal atomic ratio after the enhanced WGSR increased to 0.58 with Mg(OH)$_2$, 0.78 with Ca(OH)$_2$, 0.06 with Mg$_2$SiO$_4$, and 0.1 with CaSiO$_3$, respectively. In terms of the carbonate fraction, the increased carbon/metal ratio of Mg$_2$SiO$_4$ requires doubling to compare with other sources due to its doubled stoichiometric coefficient of metal ion, which results in a 0.12 increase in Mg$_2$SiO$_4$ carbon/metal atomic ratio after the enhanced WGSR. In this case, the varying trend in carbon/metal atomic ratio increases perfectly aligns with the enhanced WGSR: Ca(OH)$_2$ > Mg(OH)$_2$ > Mg$_2$SiO$_4$ > CaSiO$_3$, indicating the strong positive correlation between the enhanced H$_2$ yields and carbonate formation.

3.8 Insights on the mechanisms of the enhanced WGSR and *in situ* CO$_2$ capture and carbon mineralization

Given the multiphase reaction described in Fig. 1, the key reaction mechanisms involved in the enhanced WGSR can be delineated as CO oxidation and CO$_2$ capture. To be more specific, the CO oxidation proceeds *via* two potential approaches simultaneously: (i) the gaseous-phase WGSR with the assistance of noble-metal (Pt/Al$_2$O$_3$) catalyst (eqn (1)) and (ii) the aqueous-phase CO reaction to form formate followed by subsequent formate decomposition (eqn (14) and (15)).[108]

$$CO_{(aq)} + OH^-_{(aq)} \rightarrow HCOO^-_{(aq)} \qquad (14)$$

$$HCOO^-_{(aq)} + H_2O_{(aq)} \rightarrow CO_{2(g)} + H_{2(g)} + OH^-_{(aq)} \qquad (15)$$

The first mechanism results in maximum H$_2$ production, while the second mechanism consumes part of the CO supply yet may not produce H$_2$ eventually due to the limitation of formate decomposition. It is well-reported that the reaction between CO and hydroxide species leads to a competition between CO and CO$_2$ dissolution in the second mechanism. According to previous studies, higher CO partial pressure in the system may result in a larger amount of expelled CO$_2$ from the solution and restrict the subsequent carbon

mineralization step.[109] In this situation, the alkalinity of the slurry becomes an essential factor of the aqueous-phase CO oxidation: more sufficient hydroxide ion supply alleviates the competition between CO and CO_2 and promotes both H_2 production and CO_2 capture, which explains the enhancement in performance of hydroxide in this study when compared to their silicate counterparts (Fig. 6). Additionally, to evaluate the impact of the non-decomposed formate, the separated aqueous phase after reactions are characterized by liquid-state nuclear magnetic resonance (NMR), as shown in Table S3.† Although the blank experiment without alkaline sorbent exhibits a relatively high residual formate level in the aqueous phase, only trace amounts of formate (<200 ppm) were detected in the aqueous phase when alkaline resources were applied. The observation indicates the presence of alkaline sorbents effectively catalyzes the decomposition of the generated formate, leading to the near-complete oxidization of dissolved CO into CO_2.

On the other hand, the generated CO_2 from both CO oxidation mechanisms further hydrated to form bicarbonate and carbonate species and released protons into the aqueous phase (eqn (16)).[110] Simultaneously, the dissolution of the alkaline resources released the metal cations (M^{2+}), which could be enhanced by the increasing proton level. Consequently, the metal cations combine with carbonate species (CO_3^{2-}, HCO_3^-) precipitated out when the solubility limit is reached (eqn (17)). In our case, the carbonate products tend to be in anhydrous form due to their favored chemical stability at the operating temperature (250–300 °C) in this multiphase reaction environment,[111] which is also confirmed by the characterization of the solid products.

$$CO_{2(aq)} + H_2O_{(l)} \rightarrow HCO_{3(aq)}^- + H_{(aq)}^+ \rightarrow CO_{3(aq)}^{2-} + 2H_{(aq)}^+ \quad (16)$$

$$M_{(aq)}^{2+} + CO_{3(aq)}^{2-} \rightarrow MCO_{3(s)} \quad (17)$$
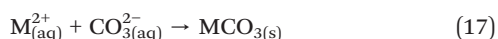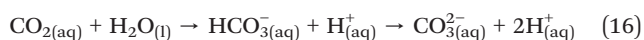
4. Conclusions

In this study, the feasibility of the enhanced WGSR integrated with *in situ* thermodynamically downhill CO_2 capture and mineralization is investigated in the presence of Mg- and Ca-hydroxides and silicates to co-produce H_2 and carbonate-bearing materials. Calibrated tuning of the multiphase chemical interactions is unlocked by deriving the thermodynamical models of the multiphase reactions, where the theoretical prediction of the CO conversion is mutually corroborated with the experimental results. For example, 30.82% more H_2 yields with 20.17% less CO_2 emission achieved with $Ca(OH)_2$ compared with independent WGS reaction without *in situ* CO_2 capture and mineralization. Thus, these studies proved the hypothesis that the *in situ* capture and mineralization of gaseous CO_2 depletes CO_2 gas compositions and favors the forward reaction to produce H_2. The higher solubility and dissolution rates of Ca- and Mg-

hydroxides favors enhanced H_2 yields. Comparable compositions of H_2 are achieved with $Mg(OH)_2$ and Mg_2SiO_4 when reacted for 12 hours at 300C despite initial slower kinetics of CO conversion with Mg_2SiO_4 in the first 6 hours of the reaction.

Among the studied alkaline resources for enhanced WGSR, $Ca(OH)_2$ exhibited unbeatable CO_2 capture over the other sorbents (CO_2 compositions: $Ca(OH)_2$ (4.22%) < $Mg(OH)_2$ (14.48%) < Mg_2SiO_4 (20.7%) < $CaSiO_3$ (22.45%) < blank experiment (24.39%) respectively), when feeding a mixture of CO and N_2 at 300 °C and 20 bar. Additionally, the temporal evolution in H_2 yields and CO_2 capture revealed that the kinetic limitation of the overall reaction was dependent on the sorbent dissolution behavior, especially for the silicate sorbents. The amorphous Si-rich layer generated from silicate dissolution and mineralization passivated the alkaline resources and restricted the rate of enhanced WGSR, particularly in the case of $CaSiO_3$. The dissolution of Mg- and Ca-bearing hydroxides and silicates, formation of the silica passivation layer, and anhydrous metal carbonate products in the reacted alkaline resources are confirmed from structural and morphological analyses. Detailed characterization and analyses confirmed that anhydrous carbonates ($MgCO_3$, $CaCO_3$) are the dominant carbonate – bearing products without any associated hydrated carbonate formations. Quantitative analyses of the reacted products showed that the carbonate content corresponded directly to the trend in H_2 yields. Evidence of comparable H_2 yields with Mg_2SiO_4 and $Mg(OH)_2$ indicates the feasibility of directly using silicates for enhanced WGSR as opposed to extracting $Mg(OH)_2$ from Mg_2SiO_4 resources, thus enabling more material and energy efficient pathways for producing H_2 with inherent CO_2 capture and storage in the form on durable Mg- and Ca-bearing carbonates. This approach can also unlock new opportunities in harnessing renewable biomethane for co-producing H_2 with inherent CO_2 capture and mineralization to produce carbonates for use in construction materials by harnessing energy from renewable sources, thus enabling carbon-negative pathways for a sustainable energy and resource future.

Data availability

The data supporting this article have been included in the main manuscript and as part of the ESI.†

Author contributions

Greeshma Gadikota – supervision, conceptualization, data curation, formal analysis, funding acquisition, investigation, methodology, project administration, resources, software, validation, visualization, writing – original draft, writing – review & editing. Xun Gao – conceptualization, data curation, formal analysis, investigation, methodology, resources, software, validation, visualization, writing – original draft, writing – review & editing; Divya Prasad – investigation,

This journal is © The Royal Society of Chemistry 2025

React. Chem. Eng., 2025, **10**, 576–592 | **589**

validation, visualization, writing – review & editing; Mahadeo A. Mahadik – investigation, validation, visualization, writing – review & editing.

Conflicts of interest

Greeshma Gadikota is the co-founder of Carbon To Stone which is commercializing technologies for industrial decarbonization and carbon management. The other authors declare that they have no known competing financial interests or personal relationships that could have appeared to influence the work reported in this paper.

Acknowledgements

References

1 R. E. H. Sims, H. H. Rogner and K. Gregory, *Energy Policy*, 2003, **31**, 1315–1326.

2 International Energy Agency (IEA), *Global Energy Review: CO₂ Emissions in 2021*, IEA, 2022.

3 D. Prasad, K. N. Patil, N. K. Chaudhari, H. Kim, B. M. Nagaraja and A. H. Jadhav, *Catal. Rev.: Sci. Eng.*, 2022, **64**, 356–443.

4 M. A. Rosen and S. Koohi-Fayegh, *Energy, Ecol. Environ.*, 2016, **1**, 10–29.

5 M. A. Pellow, C. J. M. Emmott, C. J. Barnhart and S. M. Benson, *Energy Environ. Sci.*, 2015, **8**, 1938–1952.

6 I. K. Kapdan and F. Kargi, *Enzyme Microb. Technol.*, 2006, **38**, 569–582.

7 P. Nikolaidis and A. Poullikkas, *Renewable Sustainable Energy Rev.*, 2017, **67**, 597–611.

8 J. D. Holladay, J. Hu, D. L. King and Y. Wang, *Catal. Today*, 2009, **139**, 244–260.

9 M. I. Temkin, *Adv. Catal.*, 1979, **28**, 173–287.

10 C. Rhodes, G. J. Hutchings and A. M. Ward, *Catal. Today*, 1995, **23**, 43–58.

11 C. Ratnasamy and J. P. Wagner, *Catal. Rev.:Sci. Eng.*, 2009, **51**, 325–440.

12 H. Bohlbro, *J. Catal.*, 1964, **3**, 207–215.

13 W. Xu, R. Si, S. D. Senanayake, J. Llorca, H. Idriss, D. Stacchiola, J. C. Hanson and J. A. Rodriguez, *J. Catal.*, 2012, **291**, 117–126.

14 P. Mierczynski, W. Maniukiewicz and T. P. Maniecki, *Cent. Eur. J. Chem.*, 2013, **11**, 912–919.

15 D. W. Jeong, W. J. Jang, J. O. Shim, W. B. Han, H. S. Roh, U. H. Jung and W. L. Yoon, *Renewable Energy*, 2014, **65**, 102–107.

16 X. Zhang, M. Zhang, Y. Deng, M. Xu, L. Artiglia, W. Wen, R. Gao, B. Chen, S. Yao, X. Zhang, M. Peng, J. Yan, A. Li, Z. Jiang, X. Gao, S. Cao, C. Yang, A. J. Kropf, J. Shi, J. Xie, M. Bi, J. A. van Bokhoven, Y. W. Li, X. Wen, M. Flytzani-Stephanopoulos, C. Shi, W. Zhou and D. Ma, *Nature*, 2021, **589**, 396–401.

17 L. Chen, Z. Qi, S. Zhang, J. Su and G. A. Somorjai, *Catalysts*, 2020, **10**, 858.

18 E. R. Van Selow, P. D. Cobden, P. A. Verbraeken, J. R. Hufton and R. W. Van Den Brink, *Ind. Eng. Chem. Res.*, 2009, **48**, 4184–4193.

19 J. Gibbins and H. Chalmers, *Energy Policy*, 2008, **36**, 4317–4322.

20 I. Sreedhar, T. Nahar, A. Venugopal and B. Srinivas, *Renewable Sustainable Energy Rev.*, 2017, **76**, 1080–1107.

21 R. Ben-Mansour, M. A. Habib, O. E. Bamidele, M. Basha, N. A. A. Qasem, A. Peedikakkal, T. Laoui and M. Ali, *Appl. Energy*, 2016, **161**, 225–255.

22 R. Khalilpour, K. Mumford, H. Zhai, A. Abbas, G. Stevens and E. S. Rubin, *J. Cleaner Prod.*, 2015, **103**, 286–300.

23 C. A. Scholes, M. T. Ho, D. E. Wiley, G. W. Stevens and S. E. Kentish, *Int. J. Greenhouse Gas Control*, 2013, **17**, 341–348.

24 A. Sanna, M. Uibu, G. Caramanna, R. Kuusik and M. M. Maroto-Valer, *Chem. Soc. Rev.*, 2014, **43**, 8049–8080.

25 H. M. Jang, K. B. Lee, H. S. Caram and S. Sircar, *Chem. Eng. Sci.*, 2012, **73**, 431–438.

26 S. M. Kim, A. Armutlulu, A. M. Kierzkowska, D. Hosseini, F. Donat and C. Müller, *Sustainable Energy Fuels*, 2020, **4**, 713–729.

27 M. S. Duyar, R. J. Farrauto, M. J. Castaldi and T. M. Yegulalp, *Ind. Eng. Chem. Res.*, 2014, **53**, 1064–1072.

28 C. Zhang, Y. Li, Z. He, J. Zhao and D. Wang, *Appl. Catal., B*, 2022, **314**, 121474.

29 T. Noor, M. V. Gil and D. Chen, *Appl. Catal., B*, 2014, **150–151**, 585–595.

30 R. W. Stevens, A. Shamsi, S. Carpenter and R. Siriwardane, *Fuel*, 2010, **89**, 1280–1286.

31 Y. Hu, H. Cui, Z. Cheng and Z. Zhou, *Chem. Eng. J.*, 2019, **377**, 119823.

32 C. H. Lee and K. B. Lee, *Appl. Energy*, 2017, **205**, 316–322.

33 S. Sun, C. Zhang, S. Chen, X. Zhao, Y. Wang, S. Xu and C. Wu, *R. Soc. Open Sci.*, 2023, **10**, 230067.

34 K. S. Lackner, C. H. Wendt, D. P. Butt, E. L. Joyce and D. H. Sharp, *Energy*, 1995, **20**, 1153–1170.

35 D. E. Giammar, R. G. Bruant and C. A. Peters, *Chem. Geol.*, 2005, **217**, 257–276.

36 P. B. Kelemen, R. Aines, E. Bennett, S. M. Benson, E. Carter, J. A. Coggon, J. C. De Obeso, O. Evans, G. Gadikota, G. M. Dipple, M. Godard, M. Harris, J. A. Higgins, K. T. M. Johnson, F. Kourim, R. Lafay, S. Lambart, C. E. Manning, J. M. Matter, K. Michibayashi, T. Morishita, J. Noël, K. Okazaki, P. Renforth, B. Robinson, H. Savage, R. Skarbek, M. W. Spiegelman, E. Takazawa, D. Teagle, J. L. Urai and J. Wilcox, in *Energy Procedia*, Elsevier Ltd, 2018, vol. 146, pp. 92–102.

590 | *React. Chem. Eng.*, 2025, **10**, 576–592

This journal is © The Royal Society of Chemistry 2025

37 B. P. McGrail, H. T. Schaef, A. M. Ho, Y. J. Chien, J. J. Dooley and C. L. Davidson, *J. Geophys. Res.:Solid Earth*, 2006, **111**, 1–13.

38 K. S. Lackner, *Annual Review of Energy and the Environment*, 2002, **27**, 193–232.

39 G. Gadikota, J. Matter, P. Kelemen and A. H. A. Park, *Phys. Chem. Chem. Phys.*, 2014, **16**, 4679–4693.

40 G. Gadikota, J. Matter, P. Kelemen, P. V. Brady and A. H. A. Park, *Fuel*, 2020, **277**, 117900.

41 G. Gadikota, E. J. Swanson, H. Zhao and A. H. A. Park, *Ind. Eng. Chem. Res.*, 2014, **53**, 6664–6676.

42 R. Baciocchi, G. Costa, A. Polettini, R. Pomi and V. Prigiobbe, *Energy Procedia*, 2009, **1**, 4851–4858.

43 R. Zevenhoven, S. Teir and S. Eloneva, *Energy*, 2008, **33**, 362–370.

44 C. R. Müller, R. Pacciani, C. D. Bohn, S. A. Scott and J. S. Dennis, *Ind. Eng. Chem. Res.*, 2009, **48**, 10284–10291.

45 E. R. van Selow, P. D. Cobden, A. D. Wright, R. W. van den Brink and D. Jansen, *Energy Procedia*, 2011, **4**, 1090–1095.

46 Y. Liu, Z. Li, L. Xu and N. Cai, *Ind. Eng. Chem. Res.*, 2012, **51**, 11989–11997.

47 J. Boon, K. Coenen, E. van Dijk, P. Cobden, F. Gallucci and M. van Sint Annaland, *Adv. Chem. Eng.*, 2017, **51**, 3–96.

48 D. Iruretagoyena, K. Hellgardt and D. Chadwick, *Int. J. Hydrogen Energy*, 2018, **43**, 4211–4222.

49 T. J. Stadler, P. Barbig, J. Kiehl, R. Schulz, T. Klövekorn and P. Pfeifer, *Energies*, 2021, **14**, 355.

50 J. Fagerlund, J. Highfield and R. Zevenhoven, *RSC Adv.*, 2012, **2**, 10380–10393.

51 L. Zhao, L. Sang, C. Jun, J. Ji and H. H. Teng, *Environ. Sci. Technol.*, 2010, **44**, 406–411.

52 A. I. Fernández, J. M. Chimenos, M. Segarra, M. A. Fernández and F. Espiell, *Hydrometallurgy*, 1999, **53**, 155–167.

53 W. K. O'Connor, D. C. Dahlin, G. E. Rush, S. J. Gerdemann, L. R. Penner and R. P. Nilsen, *Aqueous Mineral Carbonation: Mineral Availability, Pretreatment, Reaction Parametrics, and Process Studies, DOE/ARC-TR-04-002*, Albany Research Center, Albany, 2005.

54 A. I. Fernández, J. M. Chimenos, M. Segarra, M. A. Fernández and F. Espiell, *Hydrometallurgy*, 1999, **53**, 155–167.

55 J. S. Loring, C. J. Thompson, C. Zhang, Z. Wang, H. T. Schaef and K. M. Rosso, *J. Phys. Chem. A*, 2012, **116**, 4768–4777.

56 W. J. J. Huijgen, G. J. Witkamp and R. N. J. Comans, *Environ. Sci. Technol.*, 2005, **39**, 9676–9682.

57 G. Gadikota, *Nat. Rev. Chem.*, 2020, **4**, 78–89.

58 M. Bilal and S. D. Jackson, *Appl. Catal., A*, 2017, **529**, 98–107.

59 R. Y. Chein, Y. H. Lin, Y. C. Chen, Y. P. Chyou and J. N. Chung, *Int. J. Hydrogen Energy*, 2014, **39**, 18854–18862.

60 I. Kocemba, I. Śmiechowicz, M. Jędrzejczyk, J. Rogowski and J. M. Rynkowski, *Catalysts*, 2021, **11**, 1475.

61 E. Baraj, K. Ciahotný and T. Hlinčík, *Fuel*, 2021, **288**, 119817.

62 P. Ochonma, C. Noe, S. Mohammed, A. Mamidala and G. Gadikota, *React. Chem. Eng.*, 2023, **8**, 1943–1959.

63 B. R. Smith, J. M. Loganathan and M. Shekhar Shantha, *Int. J. Chem. React. Eng.*, 2010, **8**, 1–32.

64 K. J. Fricker, Magnesium Hydroxide Sorbents for Combined Carbon Dioxide Capture and Storage In Energy Conversion Systems, *PhD Thesis*, Columbia University, 2014.

65 D. P. Harrison, *Ind. Eng. Chem. Res.*, 2008, **47**, 6486–6501.

66 E. Abbasi, A. Hassanzadeh, S. Zarghami, H. Arastoopour and J. Abbasian, *Fuel*, 2014, **137**, 260–268.

67 J. L. Palandri and Y. K. Kharaka, *Open-File Rep. – U. S. Geol. Surv.*, 2004, **1068**, 1–64.

68 B. Li, L. Wei, H. Yang, X. Wang and H. Chen, *Energy*, 2014, **68**, 248–254.

69 Z. Giergiczny, *Cem. Concr. Res.*, 2019, **124**, 105826.

70 A. Polat, P. W. U. Appel and B. J. Fryer, *Gondwana Res.*, 2011, **20**, 255–283.

71 S. V. Golubev, O. S. Pokrovsky and J. Schott, *Chem. Geol.*, 2005, **217**, 227–238.

72 G. Rim, A. K. Marchese, P. Stallworth, S. G. Greenbaum and A.-H. A. Park, *Chem. Eng. J.*, 2020, **396**, 125204.

73 S. Katre, P. Ochonma, H. Asgar, A. M. Nair, K. Ravi and G. Gadikota, *Phys. Chem. Chem. Phys.*, 2024, **26**, 9264–9283.

74 S. J. Gerdemann, W. K. O'Connor, D. C. Dahlin, L. R. Penner and H. Rush, *Environ. Sci. Technol.*, 2007, **41**, 2587–2593.

75 R. Kurosawa, M. Takeuchi and J. Ryu, *RSC Adv.*, 2021, **11**, 24292–24311.

76 W. Liang, Y. Yin, L. Wang, L. Chen and H. Li, *J. Alloys Compd.*, 2017, **702**, 346–351.

77 Z. F. Cheng, X. Hu, Y. Li and Z. Y. Ling, *J. Am. Ceram. Soc.*, 2016, **99**, 2688–2692.

78 Y. H. Lee, H. Eom, S. M. Lee and S. S. Kim, *RSC Adv.*, 2021, **11**, 8306–8313.

79 H. Zheng, Y. He, Y. Zhu, L. Liu and X. Cui, *RSC Adv.*, 2021, **11**, 12476–12483.

80 K. S. P. Karunadasa, C. H. Manoratne, H. M. T. G. A. Pitawala and R. M. G. Rajapakse, *J. Phys. Chem. Solids*, 2019, **134**, 21–28.

81 L. Ernawati, R. A. Wahyuono, A. D. Laksono, A. Ningrum, K. Handayani and A. Sabrina, *IOP Conf. Ser.:Mater. Sci. Eng.*, 2021, **1053**, 012001.

82 R. Lakshmi, V. Velmurugan and S. Sasikumar, *Combust. Sci. Technol.*, 2013, **185**, 1777–1785.

83 T. N. Ramesh and A. Taj, *Int. J. Sci. Res.*, 2013, **1**, 58.

84 C. H. Park, J. H. Lee, E. Jang, K. B. Lee and J. H. Kim, *Chem. Eng. J.*, 2017, **307**, 503–512.

85 A. Z. Noah, M. A. El Semary, A. M. Youssef and M. A. El-Safty, *Egypt. J. Pet.*, 2017, **26**, 33–40.

86 S. H. Tamin, S. B. R. S. Adnan, M. H. Jaafar and N. S. Mohamed, *Ionics*, 2018, **24**, 2665–2671.

87 A. Saberi, B. Alinejad, Z. Negahdari, F. Kazemi and A. Almasi, *Mater. Res. Bull.*, 2007, **42**, 666–673.

88 M. V. Reddy and M. Pathak, *J. Inorg. Organomet. Polym. Mater.*, 2018, **28**, 2187–2195.

This journal is © The Royal Society of Chemistry 2025

React. Chem. Eng., 2025, **10**, 576–592 | 591

89 K. H. Tan, A. Iqbal, F. Adam, N. H. H. Abu Bakar, M. N. Ahmad, R. M. Yusop and H. Pauzi, *RSC Adv.*, 2019, **9**, 38760–38771.

90 J. P. Holgado, G. Munuera, J. P. Espinos and A. R. Gonzalez-Elipe, *Appl. Surf. Sci.*, 2000, **158**, 164–171.

91 P.-C. Huang, A. C. Vilando, T.-H. Ha and M.-C. Lu, *Sustainable Environ. Res.*, 2024, **34**, 11.

92 X. Y. Peng, X. X. Liu, D. Diamond and K. T. Lau, *Carbon*, 2011, **49**, 3488–3496.

93 Y. Xu, H. Bai, G. Lu, C. Li and G. Shi, *J. Am. Chem. Soc.*, 2008, **130**, 5856–5857.

94 C. M. Chen, J. Q. Huang, Q. Zhang, W. Z. Gong, Q. H. Yang, M. Z. Wang and Y. G. Yang, *Carbon*, 2012, **50**, 659–667.

95 A. Dufourny, C. Julcour, J. Esvan, L. Cassayre, P. Laniesse and F. Bourgeois, *Front. Clim.*, 2022, **4**, 946735.

96 B. Han, Y. Yang, J. Li, H. Deng and C. Yang, *Int. J. Electrochem. Sci.*, 2018, **13**, 9166–9182.

97 M. T. Nichols, W. Li, D. Pei, G. A. Antonelli, Q. Lin, S. Banna, Y. Nishi and J. L. Shohet, *J. Appl. Phys.*, 2014, **115**, 094105.

98 M. J. Guittet, J. P. Crocombette and M. Gautier-Soyer, *Phys. Rev. B: Condens. Matter Mater. Phys.*, 2001, **63**, 125117.

99 A. A. Khassin, T. M. Yurieva, M. P. Demeshkina, G. N. Kustova, I. Sh. Itenberg, V. V. Kaichev, L. M. Plyasova, V. F. Anufrienko, I. Yu. Molina, T. V. Larina, N. A. Baronskaya and V. N. Parmon, *Phys. Chem. Chem. Phys.*, 2003, **5**, 4025–4031.

100 H. Xu, Q. Wang, H. Xiao, X. Li, X. Su, M. Tang, L. Chen and S. Li, *RSC Adv.*, 2019, **9**, 1319–1326.

101 J. Esvan, G. Berger, S. Fabre, E. Bêche, Y. Thébault, A. Pages and C. Charvillat, *Geochim. Cosmochim. Acta*, 2022, **335**, 124–136.

102 L. Liu, J. Liu, L. Zhao, Z. Yang, C. Lv, J. Xue and A. Tang, *Environ. Sci. Pollut. Res.*, 2019, **26**, 8721–8736.

103 X. Gao, H. Asgar, I. Kuzmenko and G. Gadikota, *Microporous Mesoporous Mater.*, 2021, **327**, 111381.

104 A. Kaur, P. Chahal and T. Hogan, *IEEE Electron Device Lett.*, 2016, **37**, 142–145.

105 D. A. Shirley, High-Resolution X-Ray Photoemission Spectrum of the Valence Bands of Gold, *Phys. Rev. B: Solid State*, 1972, **5**, 4709.

106 T. V. Larina, L. S. Dovlitova, V. V. Kaichev, V. V. Malakhov, T. S. Glazneva, E. A. Paukshtis and B. S. Bal'Zhinimaev, *RSC Adv.*, 2015, **5**, 79898–79905.

107 G. Greczynski and L. Hultman, *ChemPhysChem*, 2017, **18**, 1507–1512.

108 D. C. Elliott, R. T. Hallen and L. J. Sealock, *Ind. Eng. Chem. Process Des. Dev.*, 1983, **22**, 431–435.

109 W. A. R. Slegeir, R. S. Sapienza, R. Rayford and L. Lam, *Organometallics*, 1982, **1**, 1728–1730.

110 A. H. G. Cents, D. W. F. Brilman and G. F. Versteeg, *Chem. Eng. Sci.*, 2005, **60**, 5830–5835.

111 M. Hänchen, V. Prigiobbe, R. Baciocchi and M. Mazzotti, *Chem. Eng. Sci.*, 2008, **63**, 1012–1028.

592 | *React. Chem. Eng.*, 2025, **10**, 576–592

This journal is © The Royal Society of Chemistry 2025